



# TECHNICAL NOTE

D-1093

BASE FLOW CHARACTERISTICS FOR SEVERAL FOUR-  
CLUSTERED ROCKET CONFIGURATIONS AT  
MACH NUMBERS FROM 2.0 TO 3.5

By Norman T. Musial and James J. Ward

Lewis Research Center  
Cleveland, Ohio

NATIONAL AERONAUTICS AND SPACE ADMINISTRATION  
WASHINGTON

December 1961

1

2

3

4

5

6

## NATIONAL AERONAUTICS AND SPACE ADMINISTRATION

## TECHNICAL NOTE D-1093

BASE FLOW CHARACTERISTICS FOR SEVERAL FOUR-CLUSTERED ROCKET  
CONFIGURATIONS AT MACH NUMBERS FROM 2.0 TO 3.5

By Norman T. Musial and James J. Ward

## SUMMARY

A generalized study of base flow phenomena has been conducted with four 500-pound-thrust JP-4 fuel - liquid-oxygen rocket motors installed in the base of a 12-inch-diameter cylindrical model. Data were obtained over a Mach number and nozzle pressure ratio range of 2.0 to 3.5 and 340 to 6800, respectively.

Base heat flux, gas temperature, and pressure were highest in the center of the cluster core and decreased in a radial direction. Although a maximum heat flux of 93 Btu per square foot per second was measured within the cluster core, peripheral heat fluxes were low, averaging about 5 Btu per square foot per second for all configurations. Generally base heat flux was found to be independent of Mach number over the range investigated.

Base heat flux within the cluster core was decreased by increasing motor spacing, motor extension, a combination of increasing nozzle area ratio and decreasing exit angle, and gimbaling the two side engines. Small amounts of nitrogen injected within the cluster core sharply reduced core heat flux.

## INTRODUCTION

Clustering of rocket engines offers possible advantages to the missile designer such as utilizing developed "off-the-shelf" engines to produce a given thrust level or achieving engine length reduction. However, in clustering, the problem of jet interaction and base heating arises wherein heavy heat shields may be necessary to maintain missile structural integrity and to protect missile components in the base area. This, of course, adds weight and results in reduced overall missile performance.

To date, some experimental and analytic work has been done on the base heating of clustered-rocket configurations using both solid- and

liquid-propellant engines. For example, clustered-rocket base flow characteristics are discussed in reference 1. In general, the data pertinent to clusters of four engines have been applied to specific geometries at Mach numbers less than 2.0 and with low nozzle pressure ratios (less than 400). The generalized experimental program reported herein has been undertaken to examine the base heating problem of four-cluster configurations at the higher Mach numbers (2.0 to 3.5) and at much higher nozzle pressure ratios (up to 6800). The effects of various geometric design variables such as nozzle spacing, nozzle extension, and two combinations of nozzle area ratio, exit angle, and contour were investigated. In addition, the effect of introducing low-energy nitrogen into a base region as a means of reducing the magnitude of base heating was determined.

The experimental program was conducted in the NASA Lewis 10- by 10-foot supersonic wind tunnel utilizing four 500-pound-thrust JP-4 - liquid-oxygen rocket engines. Presented herein are quantitative values of base heat flux, gas temperature, and pressure for several engine arrangements.

#### SYMBOLS

$A_e/A_t$	nozzle area ratio
$c^*$	characteristic velocity
$c_p$	specific heat of disk material, Btu/(lb)(°F)
$D_b$	base diameter, in.
$D_e$	nozzle-exit diameter, in.
$D_s$	diameter of circle through nozzle centerline, in.
$D_s/D_e$	nozzle spacing ratio
$D_t$	throat diameter, in.
$d$	disk thickness, ft
$L$	nozzle extension, distance of exit plane from base plate, in.
$L/D_e$	nozzle extension ratio
$o/f$	oxidant-fuel ratio
$P_c$	combustion-chamber pressure, lb/sq ft abs
$P_c/p_0$	engine nozzle pressure ratio
$p$	static pressure, lb/sq ft abs

$p_b$	base static pressure, lb/sq ft abs
$p_e$	nozzle-exit pressure, lb/sq ft abs
$p_0$	free-stream static pressure, lb/sq ft abs
$q$	heat flux, Btu/(sq ft)(sec)
$r$	radius
$r_b$	radius of model base, in.
$T_c$	theoretical combustion-chamber gas temperature, °F
$T_d$	disk temperature, °F
$T_g$	base gas temperature, °F
$t$	time, sec
$\alpha$	nozzle-exit half-angle, deg
$\gamma$	ratio of specific heats
$\rho$	density of disk material, lb/cu ft

#### APPARATUS AND PROCEDURE

The investigation of several four-clustered rocket configurations was conducted in the Lewis 10- by 10-foot supersonic wind tunnel at Mach 2.0 to 3.5 over a range of pressure altitudes from 47,000 to 100,000 feet. The basic exit model used in the investigation was a strut-mounted cone-cylinder body having a maximum diameter of 12 inches. The model installation is illustrated in figure 1. Rocket motors were installed in clusters of four in interchangeable base plates to vary the spacing between the motors and their extension from the base.

#### Rocket Motors

Each motor was designed to produce a nominal thrust of 500 pounds at a chamber pressure of 600 pounds per square inch absolute. The two nozzle configurations employed in the investigation are shown in figure 2. The area ratio 12.0 bell-shaped nozzle had an exit half-angle of 3° and a nozzle-exit diameter of 2.94 inches. The conical nozzle had an area ratio of 6.9, an exit half-angle of 17 $\frac{1}{2}$ °, and a nozzle-exit diameter of 2.20 inches. All motors had water-cooled jackets. A coaxial-tube injector was used in which the fuel (JP-4) is injected into the combustion

chamber through the annulus surrounding each oxidant (liquid oxygen) tube. In each injector, 97 oxidant tubes were provided. A more complete description of the coaxial-tube injector is presented in reference 2.

The rockets were maintained at steady operating conditions for approximately 10 seconds; during this period chamber pressure and oxidant-fuel ratio for each motor agreed within  $\pm 3$  percent. All data were obtained at a nominal chamber pressure of 600 pounds per square inch absolute and an oxidant-fuel ratio of 2.2. The average value of characteristic velocity  $c^*$  obtained was approximately 5400 seconds.

#### Model Variables

The variations of base geometry evaluated during the test are presented schematically in figure 3 and are summarized in the following table:

Configuration	Nozzle spacing ratio, $D_s/D_e$	Nozzle extension, in.	Nozzle extension ratio, $L/D_e$	Nozzle type	Nozzle area ratio, $A_e/A_t$	General comments
1a	2.18	$5\frac{3}{32}$	1.7326	Bell	12	
1b	↓	$2\frac{1}{16}$	.7015	↓	↓	
1c	↓	$\frac{1}{8}$	.0425	↓	↓	
2	1.67	$4\frac{1}{2}$	1.5306	↓	↓	
3	2.97	2.0	.6803	↓	↓	
4	2.22	↓	.9091	$17\frac{1}{2}^\circ$ Conical	6.9	
5	2.18	↓	.6803	Bell	12	Side engines gimbaled $7^\circ$ downward
6	2.22	↓	.9091	$17\frac{1}{2}^\circ$ Conical	6.9	Nitrogen probe installed

The nozzle extension ratio  $L/D_e$  was varied from 0.0425 to 1.7326 (figs. 3(b), (c), and (d)), and the nozzle spacing to nozzle-exit diameter  $D_s/D_e$  was varied from 1.67 to 2.97 (figs. 3(a), (e), and (f)). The effect of nozzle orientation was determined by gimbaling the engines numbered two and four downward  $7^\circ$  (fig. 3(h)). The bell nozzles and conical nozzles were designed with discharge angles of  $3^\circ$  and  $17\frac{1}{2}^\circ$ , respectively.

In addition to these geometric variables, the effect of discharging nitrogen gas in the base region was determined for the configuration employing the conical nozzles. A sketch of the configuration employing nitrogen gas injection and the installation of this secondary nozzle in the center of the base are shown in figure 4.

#### Model Instrumentation

The type and location of the instrumentation mounted on the base plate for each of the configurations are shown in the sketches of figures 3 and 4. All base plates were uncooled and coated with an aluminum oxide insulation. In each case the instrumentation included static-pressure orifices, thermocouples, and disk calorimeters. Base static pressures were measured by pressure transducers. Gas temperatures in the base region were measured by bayonet-type platinum-rhodium thermocouples (fig. 5(a)) which extended  $1/2$  inch from the base plate. Gas temperature data are presented in ratio form as  $T_g/T_c$ , where  $T_g$  is the measured local gas temperature and  $T_c$  is the theoretical combustion-chamber gas temperature. An average value of  $T_c$  was used in the ratio and was determined in the following manner: The theoretical values of  $c^*$  and  $T_c$  were selected from references 3 and 4 for both frozen and equilibrium flow. The average  $T_c$  between frozen and equilibrium flow was then determined, and this value was corrected for actual measured  $c^*$  efficiency. The correction was made by multiplying the average  $T_c$  value by the square of the ratio of the measured  $c^*$  to the average theoretical  $c^*$ . This procedure resulted in a  $T_c$  value of  $5350^\circ$  F. No attempt was made to correct the measured gas temperatures for radiation losses.

Disk calorimeters (fig. 5(b)) were used to measure the total heat flux to the base region. The calorimeters consisted of either 0.050-inch- or 0.100-inch-thick copper disks, 0.375 inch in diameter, supported in a threaded stainless-steel mounting assembly. In order to minimize heat conduction losses the disks were attached to the mounting stud at only three places by stainless-steel wires. An insulating air gap was thereby maintained between the disk and the mounting stud. The two wires of an iron-constantan thermocouple were embedded in the disk and passed through the mounting assembly in ceramic tubes. An additional tube was provided in the mounting stud to admit air into the region behind the disk. The air then flowed out through the annular area between the edge of the disk and the mounting stud. The air served a dual purpose; it

maintained the disk at a constant temperature until the rockets reached operating conditions and also prevented products of combustion from depositing on the surface of the disk during the rocket starting cycle. A typical temperature-time history of a disk calorimeter is presented in figure 6. A plot of engine chamber pressure against time is presented on the same figure to provide a reference base. Disk cooling air on and off points are also indicated on the figure. Disk temperatures were recorded 100 times a second, while other engine parameters were recorded every 2.7 seconds.

Heat flux was calculated every 3/4 of a second from the slope of the disk temperature-time curve by the equation  $q = (\rho c_p d)_{\text{disk}} (dT_d/dt)$  where  $\rho$ ,  $c_p$ , and  $d$  are the disk density, specific heat, and thickness, which are constants for any particular disk at a given temperature. A typical variation of heat flux with time is shown in figure 6. The values of heat flux presented in this report correspond to the maximum measured values for a given data point. The peak heat fluxes were measured at an average value of disk temperature of 150° F.

## RESULTS AND DISCUSSION

The base flow phenomena associated with a typical four-cluster rocket configuration are illustrated in figure 7. At low nozzle pressure ratios (low altitude) the turbulent mixing boundaries of the expanding exhaust jets do not impinge on each other (fig. 7(a)). Under these conditions, the exhaust jets act as ejectors, pulling free-stream air into the base region by their aspiration action. This aspiration results in relatively flat radial profiles and low values of base flow parameters (base heat flux, gas temperature, and pressure).

Increasing altitude and thus nozzle pressure ratio causes the exhaust jets to expand. At some nozzle pressure ratio the mixing boundaries of the exhaust jets impinge on one another (fig. 7(b)). At the point of interaction the radially expanding exhaust flow is forced to change direction, thus forming trailing shock waves and an attendant wake pressure rise. Some of the low-energy gas within the mixing region of the exhaust jets is unable to negotiate this wake pressure rise. A stagnation condition will exist at the point of interaction, and a portion of the hot gas is actually turned and flows forward into the base. This reverse flow will then stagnate on the base at the center of the core (shown by the crosshatched area (fig. 7(a))) and be turned radially outward between the engines as it reaccelerates to ambient pressure. In this transitional flow regime, wake pressure rise (and thus the reverse flow) increases with increasing nozzle pressure ratio until choke conditions are reached (fig. 7(c)). The choke location may occur along the sides between the engines or in the vicinity of the nozzle-exit plane, depending on the configuration geometry (i.e., nozzle arrangement and extension). The level of base

flow parameters is highest at choke conditions with the maximum occurring at the stagnation point in the cluster core and decreasing radially out toward the periphery. Once choking is achieved, base heating should be independent of further increases in altitude.

#### Effect of Mach Number

The effect of Mach number on core and peripheral heat flux is shown in figure 8 for a configuration having a spacing ratio of 1.67 and an extension ratio of 1.5306. The greatest effect of Mach number would be expected to occur on the periphery where free-stream air has a greater opportunity to dilute the reverse flow from the rocket exhaust. As shown, the peripheral heat flux remained relatively constant for all Mach numbers. The core heat flux, on the other hand, while highly sensitive to nozzle pressure ratio, was also independent of Mach number, based on the overlapping and continuity of data through these various speeds. In this limited range then Mach number was considered to have no effect on base heating.

#### Effect of Nozzle Extension

The effect of nozzle extension on the base parameters is illustrated in figures 9 to 12. Data are presented for configurations having nozzle extension ratios of 1.7326, 0.7015, and 0.0425, respectively, and a common nozzle spacing ratio of 2.18. The variation of base heat flux, gas temperature ratio, and pressure along the base diameter is presented in figures 9 to 11 over a range of nozzle pressure ratios. Also indicated on the figures is the radius ratio identifying nozzle centerline locations. At a given nozzle pressure ratio the peak values of the parameters occur at the center of the core and decrease with increasing radius. As nozzle pressure ratio (or altitude) is increased, the level of the heat flux and gas temperature across the base initially increases while the pressure decreases.

When a core to peripheral pressure ratio sufficient to choke the flow between the engines is reached, the values of the base parameters are unaffected by further increases in nozzle pressure ratio. An exception to the general trend may be noticed in figure 10(a). At a nozzle pressure ratio of 970 the level of the temperature ratio for configuration 1a was much higher than at any of the other pressure ratios. This is indicative of base burning, and this observation was verified by movies taken during the test.

As indicated previously, nozzle cooling and radiation losses reduce the measured base gas temperatures and result in lower values of the temperature ratio than might be expected. As shown in figure 10, the maximum value of the temperature ratio obtained was approximately 0.4.

Base heat flux, gas temperature ratio, and a base pressure for each of the configurations are presented as a function of nozzle pressure ratio in figure 12. Data are presented at radius ratios  $r/r_b$  of 0.1 and 0.9 and represent the core and peripheral regions, respectively. A radius ratio of 0.1 was selected for comparison because the center ( $r/r_b = 0$ ) disk calorimeter of configuration 1c was inoperative during the test. As the nozzle extension ratio was decreased, the core heat flux increased at a given nozzle pressure ratio. For example, decreasing the nozzle extension ratio from 1.7326 to 0.0425 increased the core heat flux from 54 to 72 Btu per square foot per second at a nozzle pressure ratio of 4720 (fig. 12(a)). The peripheral heat flux was relatively unaffected by nozzle extension, and an average value of approximately 5 Btu per square foot per second was measured for the three configurations. As shown in figure 12(b) the base gas temperature ratio at the  $r/r_b = 0.1$  location increased slightly with decreasing nozzle extension, reaching a value of approximately 0.4 for the shortest nozzle extension. The level of the temperature ratio in the peripheral region was affected very little by nozzle extension and reached a value of 0.27 at a pressure ratio of 5900. The effect of base burning on the temperature ratio mentioned previously for configuration 1a at a nozzle pressure ratio of 970 is also shown. Temperatures at an  $r/r_b$  of 0.1 and 0.9 were increased to the level of the configuration 1c temperature ratio at an  $r/r_b$  of 0.1. The base pressure data of figure 13(c) indicate that, as nozzle extension was decreased, the pressure level in the core ( $r/r_b = 0.1$ ) increased while the peripheral pressure level was unaffected. Therefore reverse flow and choking of the flow between the engines occur at lower nozzle pressure ratios as nozzle extension is decreased. A core to peripheral static-pressure ratio of approximately 2.0, sufficient to choke the flow between the engines, is achieved at a nozzle pressure ratio of approximately 2500 for the 0.0425 extension ratio configuration and at a nozzle ratio of about 4500 for the 1.7326 extension ratio configuration.

#### Effect of Nozzle Spacing

The effect of nozzle spacing is presented in figures 13 to 16. Radial distributions of heat flux, gas temperature, and base pressure over a nozzle pressure ratio range are presented in figure 13 for a configuration having a nozzle spacing ratio of 1.67 and an extension ratio of 1.5306. The core heat flux and temperature ratio increased with increasing nozzle pressure ratio, and base pressure decreased until the reverse flow became choked. The maximum value of heat flux measured was 59 Btu per square foot per second at a nozzle pressure ratio of 6800 (fig. 13(a)). As with configuration 1a, an exception to the general trend is noted in regard to the gas temperature ratio at relatively low nozzle pressure ratios. The high temperatures shown at  $P_c/P_0 = 340$  indicate the presence of base burning.

The effect of decreasing nozzle spacing ratio is presented in figure 14 wherein the data from figure 13 are summarized and compared with data from figure 12 for a spacing ratio of 2.18 and an extension ratio of 1.7326. Although the extension ratios are not quite the same, it is believed the overall trends are indicative primarily of the effect of decreasing nozzle spacing. The level of all three base flow parameters in the core region increased with decreased nozzle spacing, while the values of the parameters in the peripheral region were virtually unaffected.

Radial distributions of heat flux, gas temperature, and base pressure for two nozzle pressure ratios are presented in figure 15 for a configuration having a large nozzle spacing ratio of 2.97 and an extension ratio of 0.6803. Here again the radial distributions of the base parameters are such that maximum values occur within the cluster core and decrease toward the periphery. The maximum value of heat flux in this case was on the order of 30 Btu per square foot per second.

The effect of increasing nozzle spacing ratio from 2.18 to 2.97 is presented in figure 16 wherein the data of figure 15 are summarized and compared with the data from figure 12 for a spacing ratio of 2.18 and a nozzle extension of 0.7015. In this comparison, the difference in nozzle extensions for the two spacing configurations is very small. Increasing the nozzle spacing ratio decreases the level of the base flow parameters in the core region and also influences base flow parameters in the peripheral region slightly.

#### Effect of Two Different Nozzle Geometries

The effect of varying nozzle geometry on the base flow parameters is illustrated in figures 17 and 18. Data presented previously were obtained with bell-shaped nozzles having an area ratio of 12:1 and an exit half-angle of  $3^\circ$ . To explore the effect of a different nozzle geometry on the base parameters, data were obtained with configuration 4 employing area ratio 6.9:1 conical nozzles having an exit half-angle of  $17\frac{1}{2}^\circ$ . This configuration had a nozzle spacing ratio of 2.22 and a nozzle extension ratio of 0.9091. Radial distributions of base heat flux, gas temperature ratio, and base pressure are presented in figure 17 for several nozzle pressure ratios. The base heat flux distribution (fig. 17(a)) follows the previously noted trends; base heat flux is highest in the cluster core and decreases in a radial direction. The 93-Btu-per-square-foot-per-second heating rate measured at a nozzle pressure ratio of 1465 and radial location of  $r/r_b = 0.1$  was the highest value recorded during the investigation; and, although the center ( $r/r_b = 0$ ) disk calorimeter was inoperative for this configuration, the heat loads at this location would undoubtedly be higher. Both the gas temperature ratio (fig. 17(b)) and pressure distribution (fig. 17(c)) across the base also decrease from a peak value in the core to lower values in the periphery.

The effect of a combined change in nozzle area ratio and exit angle is shown in figure 18 by comparing the data for configurations 4 and 1b at two radial locations. In this case, the parameters are plotted against nozzle static-pressure ratio to minimize the effect of area ratio; the nozzle-exit pressures were calculated from one-dimensional relations and an assumed ratio of specific heats of 1.2. The base parameters are higher in the core region for the conical nozzle configuration with the largest differences occurring in the heat flux. At a static-pressure ratio of 50, the core heat flux increases from 60 to 93 Btu per square foot per second (fig. 18(a)) when the conical nozzles are employed.

#### Effect of Nozzle Gimbaling

The data of figures 19 and 20 illustrate the effect of gimbaling the two side motors downward at  $7^\circ$ . The radial distribution of the base parameters is presented in figure 19 for configuration 5. As nozzle pressure ratio is increased, the heat loads in the upper left quadrant increase while those in the lower right quadrant decrease. In addition the heat flux level is quite low compared with the undeflected configuration 1b, reaching a peak value of only 19 Btu per square foot per second in the upper left quadrant at a nozzle pressure ratio of 3340. The peak gas temperature ratio (fig. 19(b)) also occurs in the upper left quadrant. The relatively flat pressure profile across the base (fig. 19(c)) indicates that little reverse flow is being directed back toward the base. This indicates that most of the resulting lower heat flux can be attributed to radiation from the expanding jets. Both the disk calorimeters and gas thermocouples are influenced by the form factor or solid angle of the radiative heat source. As the side nozzles are moved downward, the form factor in the upper left quadrant increases; that is, the instrumentation in this area "sees" more of the expanding jets and less of the cooler nozzle walls. The reverse is true in the lower right quadrant. Therefore, the values of the heat flux and gas temperature measured in the upper quadrant would be higher than those measured in the lower quadrant.

The base parameters of the gimbaled nozzle configuration are compared with those of the ungimbaled configuration (config. 1b) in figures 20(a) and (b) for two nozzle pressure ratios. Both the heat flux and gas temperature ratio are sharply reduced in the core region when the nozzles are gimbaled downward at  $7^\circ$ . At  $r/r_b = 0.1$  in the lower right quadrant of the base the heat flux is reduced from 60 to 10 Btu per square foot per second at a nozzle pressure ratio of approximately 3500, while at the same conditions the gas temperature ratio is reduced from 0.41 to 0.27. The base pressure distribution is also lowered slightly in the core region when the nozzles are gimbaled.

## Effect of Nitrogen Injection into Base

As is evident from the preceding sections, the heat loads in the core region of clustered rockets can be very high. Therefore, as one approach to lowering the heat load level, gaseous nitrogen was introduced into the core region of configuration 4 to determine its effectiveness. This is the configuration for which the highest heat loads were measured. The center ( $r/r_b = 0$ ) disk calorimeter of the previously mentioned configuration was replaced by a nitrogen nozzle and redesignated configuration 6.

Base heat flux distribution is presented in figure 21 for a series of nitrogen weight flows at a nozzle pressure ratio of 6600. Accompanying these data, for comparison purposes, are the no-nitrogen flow data for a nozzle pressure ratio of 1455 as previously shown in figure 17. Although there is a difference in nozzle pressure ratio, it is believed that the no-flow nitrogen data for the nozzle pressure ratio value of 6600, if available, would be at least as high as that for a nozzle pressure ratio of 1465. As shown, small amounts of nitrogen were very effective in reducing the core heat flux. A ratio of nitrogen weight flow to total engine weight flow of 0.00015 reduced the peak heat flux from an estimated 103 Btu per square foot per second at  $r/r_b = 0$  to about 52 Btu per square foot per second at  $r/r_b = 0.15$ . In the peripheral region, the heat loads were also lowered, although not as much. As the nitrogen flow was increased to 0.000955 times the total engine flow, the effectiveness in reducing the heat flux near an  $r/r_b$  of about 0.15 was reduced.

## SUMMARY OF RESULTS

A generalized study of base flow phenomena on four-cluster rocket configurations over a Mach number range of 2.0 to 3.5 and a nozzle pressure ratio range of 340 to 6800 was conducted in the Lewis 10- by 10-foot supersonic wind tunnel. The effects of various geometric design variables were assessed, and means of reducing the magnitude of base heating were determined. The following results were obtained:

1. Base heat flux in the cluster core area was found to be sensitive to nozzle pressure ratio but independent of free-stream Mach number over the range investigated.

2. Base heat flux, gas temperature, and pressure were highest in the center of the cluster and decreased with increasing radius. A maximum heat flux of 93 Btu per square foot per second was measured with the conical nozzle configuration at a radius ratio of 0.1 and minimum nozzle extension. Values of heat flux in the peripheral region were low, averaging about 5 Btu per square foot per second for all the configurations tested.

3. Increasing the nozzle extension or the nozzle spacing decreased the heating loads in the core region.

4. Gimbaling the two side motors downward at  $7^\circ$  significantly reduced the heat flux in the core while slightly increasing the heat flux in the periphery.

5. The combined effect of decreasing nozzle area ratio and increasing nozzle-exit angle increased the core heat flux.

6. Injecting small amounts of nitrogen at the center of the base of the conical nozzle configuration sharply reduced the heat flux in the core.

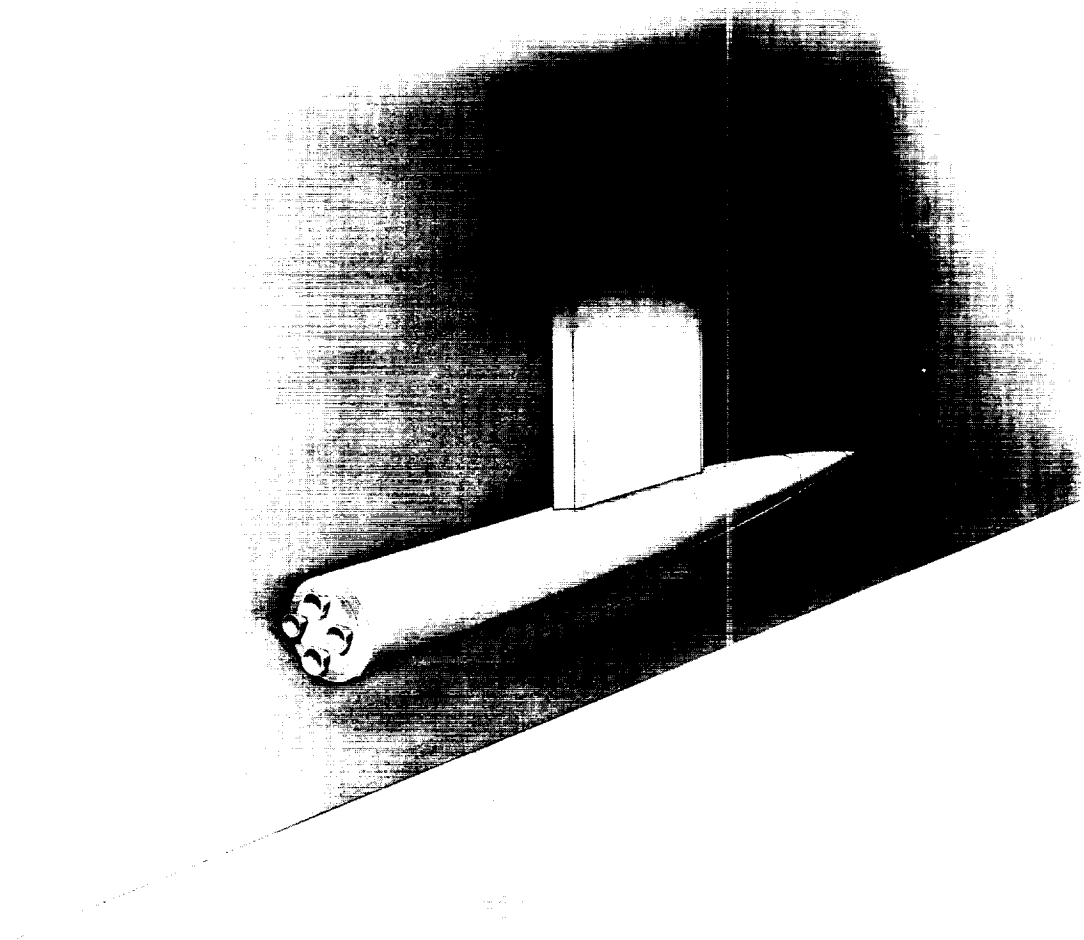
Lewis Research Center

National Aeronautics and Space Administration  
Cleveland, Ohio, July 7, 1961

## REFERENCES

1. Goethert, B. H.: Base Flow Characteristic of Missiles with Cluster-Rocket Exhausts. Aerospace Eng., vol. 20, no. 3, Mar. 1961, pp. 28-29; 108-117.
2. Stein, Samuel: A High-Performance 250-Pound-Thrust Rocket Engine Utilizing Coaxial-Flow Injection of JP-4 Fuel and Liquid Oxygen. NASA TN D-126, 1959.
3. Huff, Vearl N., and Fortini, Anthony: Theoretical Performance of JP-4 Fuel and Liquid Oxygen as a Rocket Propellant. I - Frozen Composition. NACA RM E56A27, 1956.
4. Huff, Vearl N., Fortini, Anthony, and Gordon, Sanford: Theoretical Performance of JP-4 Fuel and Liquid Oxygen as a Rocket Propellant. II - Equilibrium Composition. NACA RM E56D23, 1956.

E-1241



CD-7166

Figure 1. - Installation of exit model in 10- by 10-foot supersonic wind tunnel.

E-1241

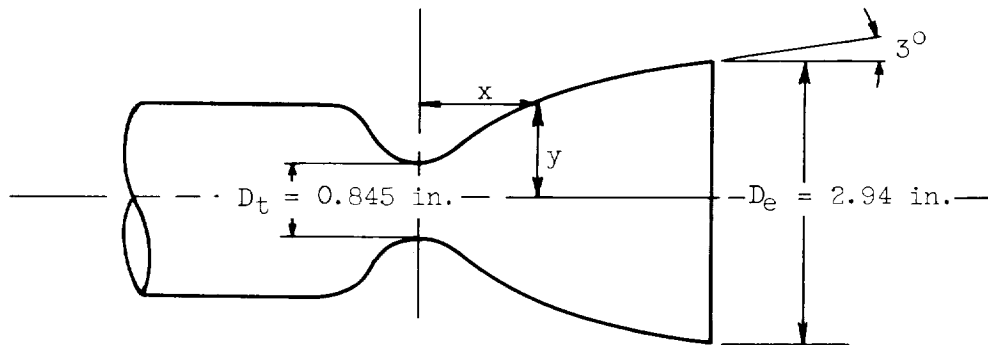
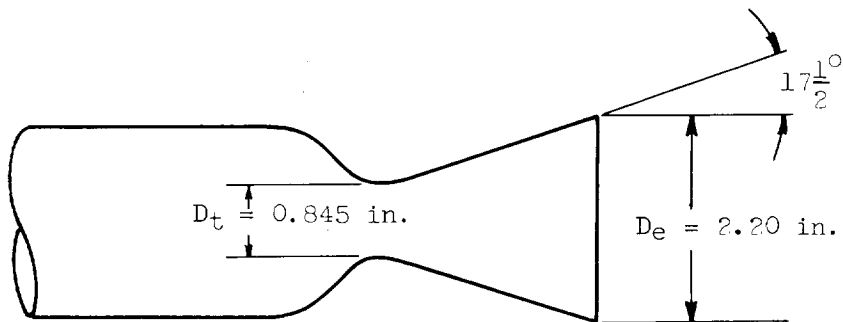


Table of coordinates	
x, in.	y, in.
0	0.4275
.5	.642
1.0	.930
1.5	1.175
2.0	1.334
2.5	1.420
3.12	1.475

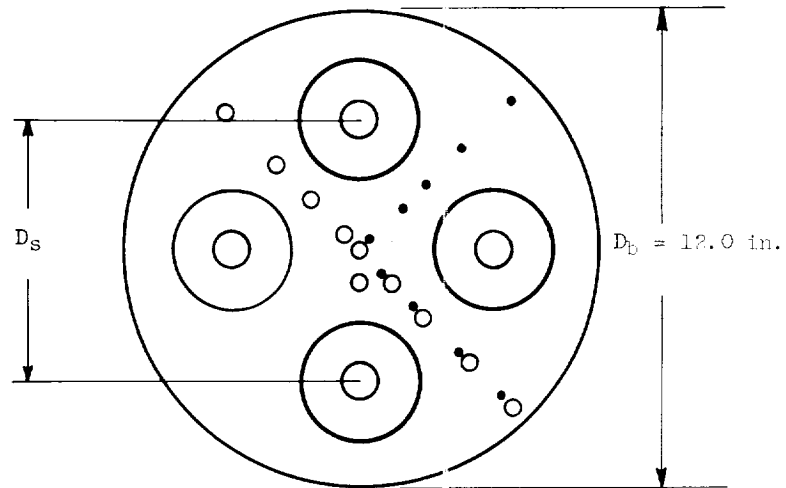
(a) Nozzle area ratio  $A_e/A_t$ , 12.0; exit half-angle  $\alpha$ ,  $3^\circ$ .



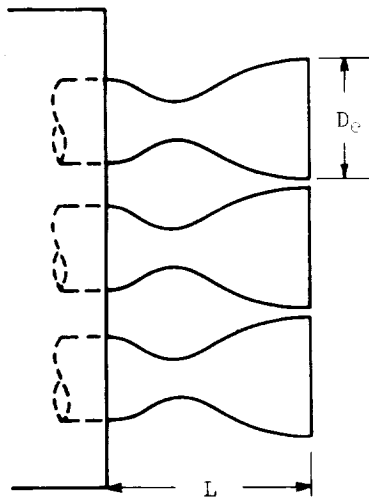
(b) Nozzle area ratio  $A_e/A_t$ , 6.9; exit half-angle  $\alpha$ ,  $17\frac{1}{2}^\circ$ .

Figure 2. - Engine configurations.

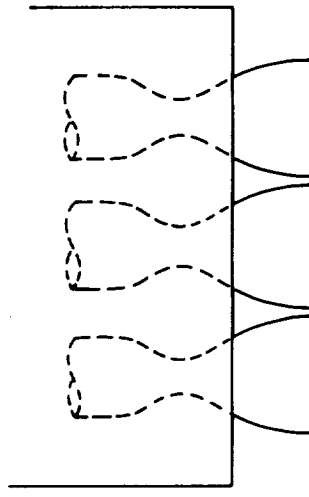
- Disk calorimeter
- Static-pressure orifice



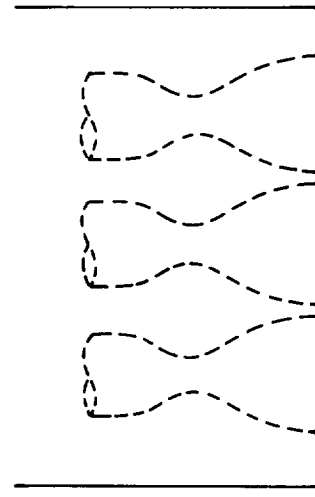
(a) Base plate instrumentation for configuration having nozzle spacing ratio  $D_s/D_e$  of 2.18.



(b) Nozzle spacing ratio  $D_s/D_e$ , 2.18; nozzle extension ratio  $L/D_e$ , 1.7326; configuration 1a.



(c) Nozzle spacing ratio  $D_s/D_e$ , 2.18; nozzle extension ratio  $L/D_e$ , 0.7015; configuration 1b.

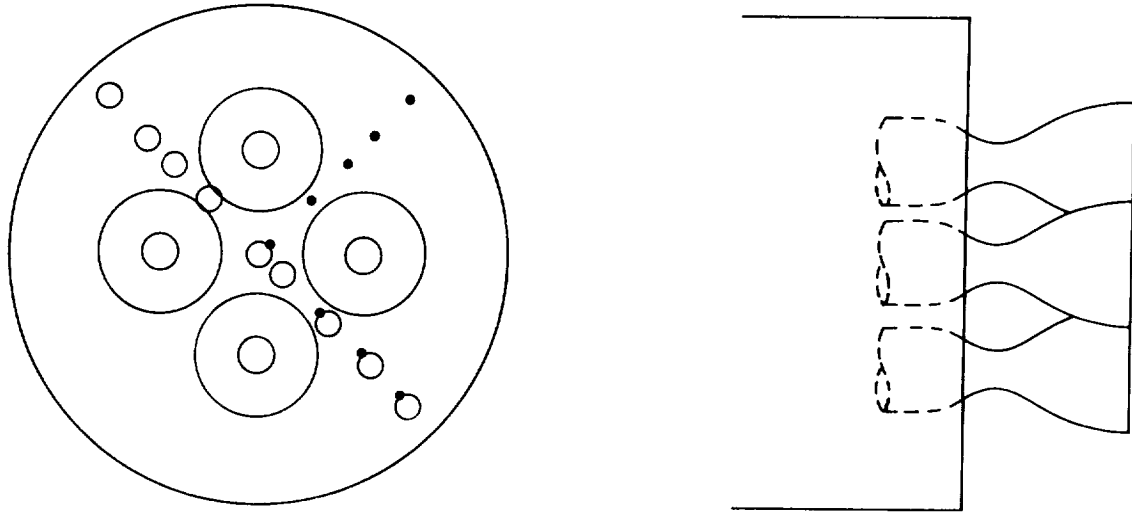


(d) Nozzle spacing ratio  $D_s/D_e$ , 2.18; nozzle extension ratio  $L/D_e$ , 0.0425; configuration 1c.

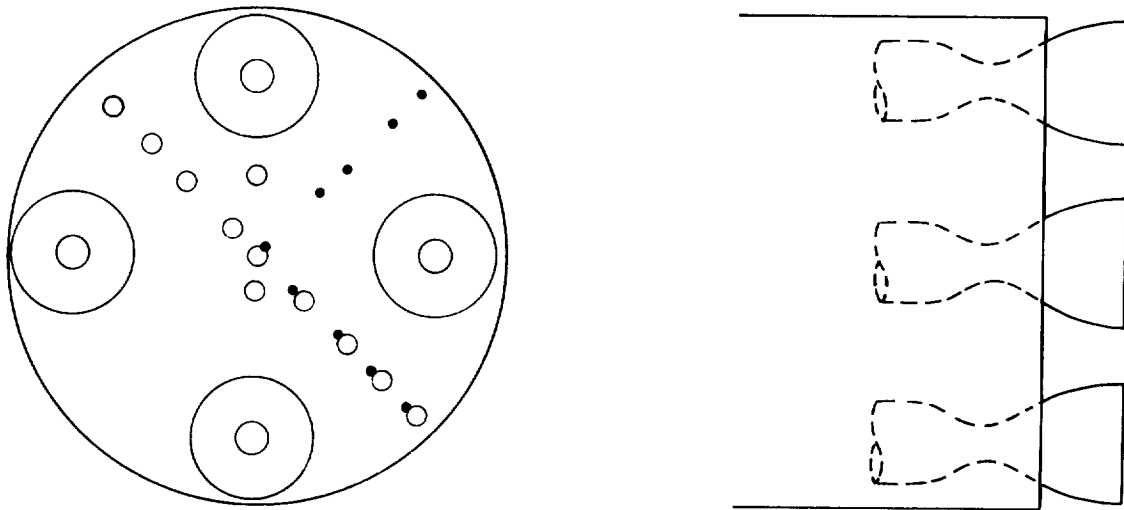
Figure 3. - Schematic diagrams illustrating geometric variables and base instrumentation for test configurations.

E-1241

- Disk calorimeter
- Static-pressure orifice

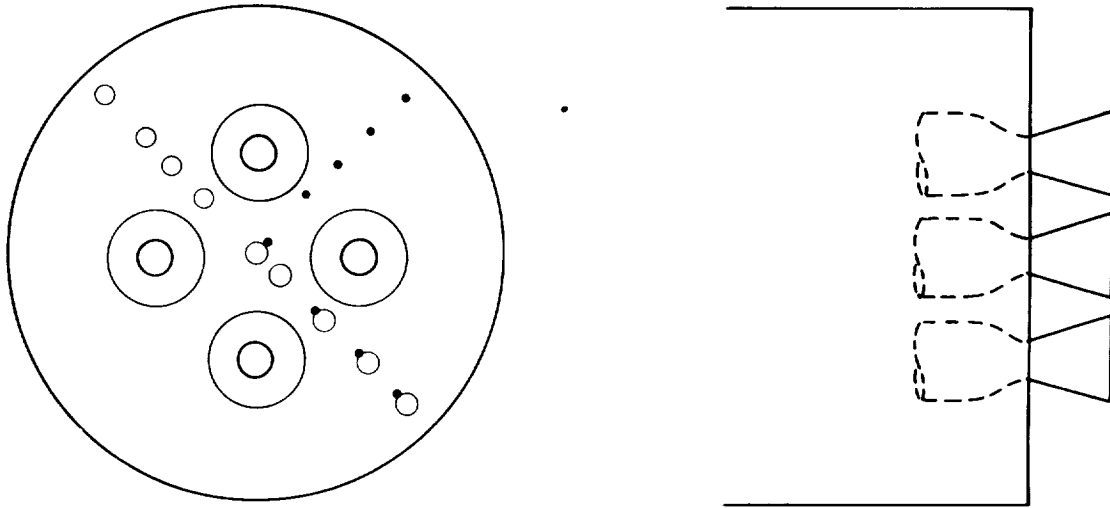


(e) Base plate instrumentation and sketch of base for configuration 2. Nozzle spacing ratio  $D_0/D_n$ , 1.67; nozzle extension ratio  $L/D_n$ , 1.5303.



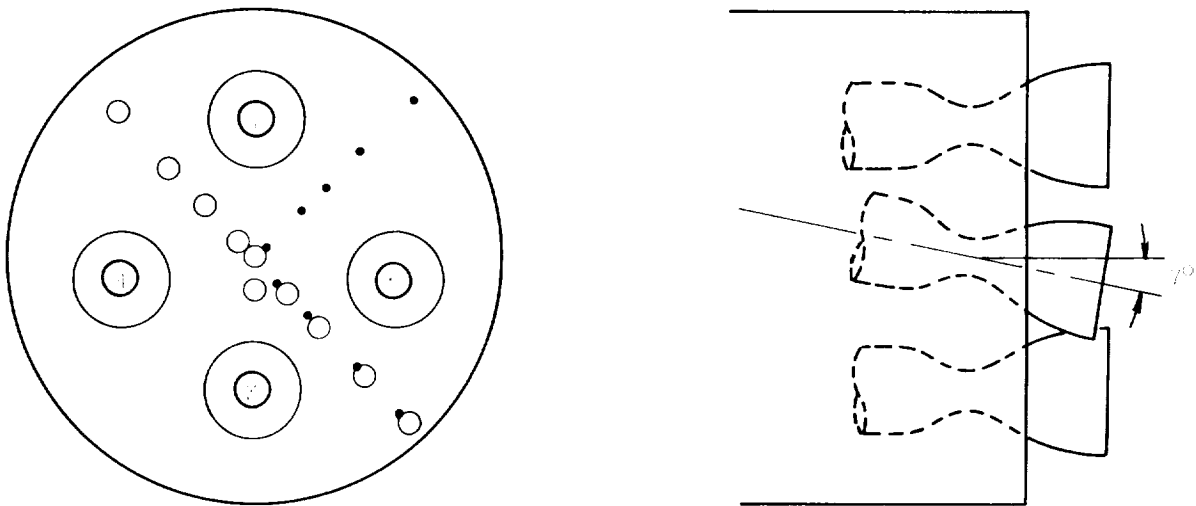
(f) Base plate instrumentation and sketch of base for configuration 3. Nozzle spacing ratio  $D_0/D_n$ , 2.07; nozzle extension ratio  $L/D_n$ , 0.6903.

Figure 3. - Continued. Schematic diagrams illustrating geometric variables and base instrumentation for test configurations.



(g) Base plate instrumentation and sketch of base for conical nozzle configuration 4. Nozzle spacing ratio  $D_S/D_e$ , 2.22; nozzle extension ratio  $L/D_e$ , 0.9091.

- Disk calorimeter
- Static-pressure orifice



(h) Base plate instrumentation and sketch of base for gimbaled nozzle configuration 5. Nozzle spacing ratio  $D_S/D_e$ , 2.18; nozzle extension ratio  $L/D_e$ , 0.9091.

Figure 3. - Concluded. Schematic diagrams illustrating geometric variables and base instrumentation for test configurations.

E-1241

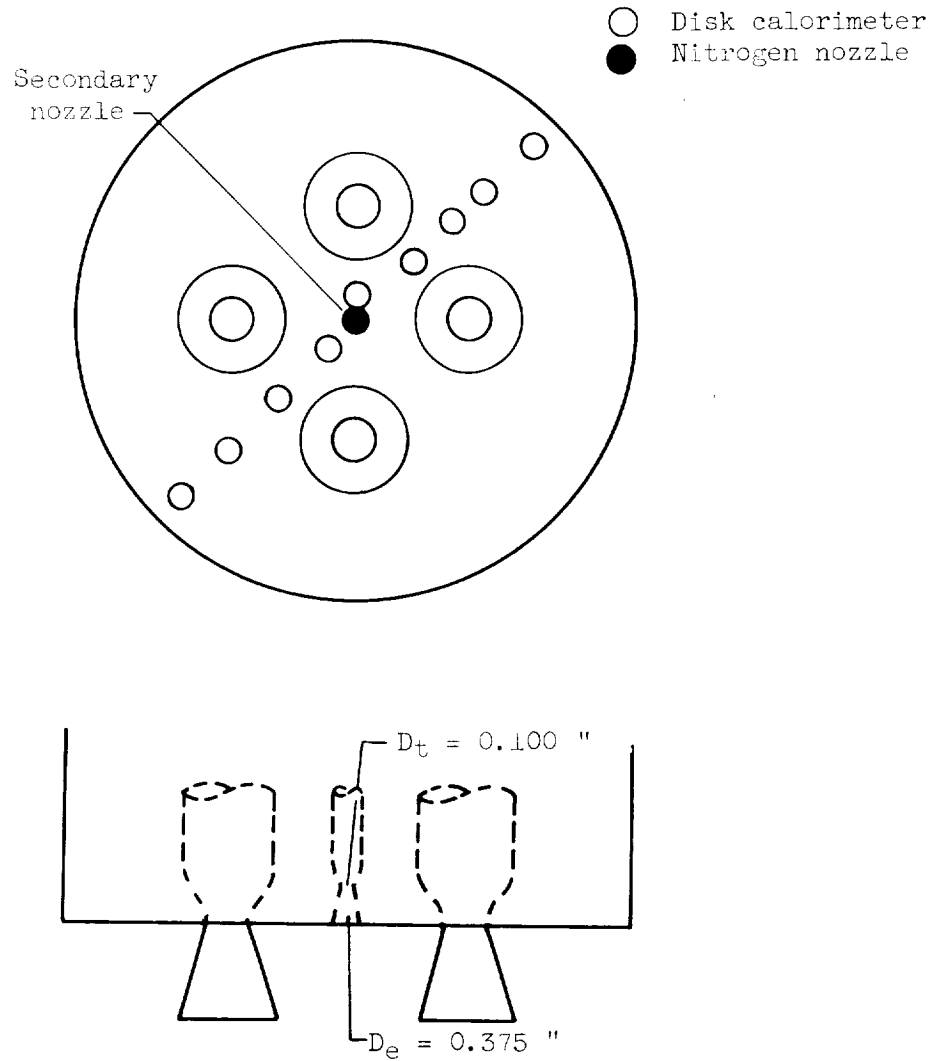
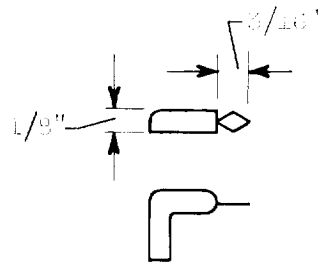
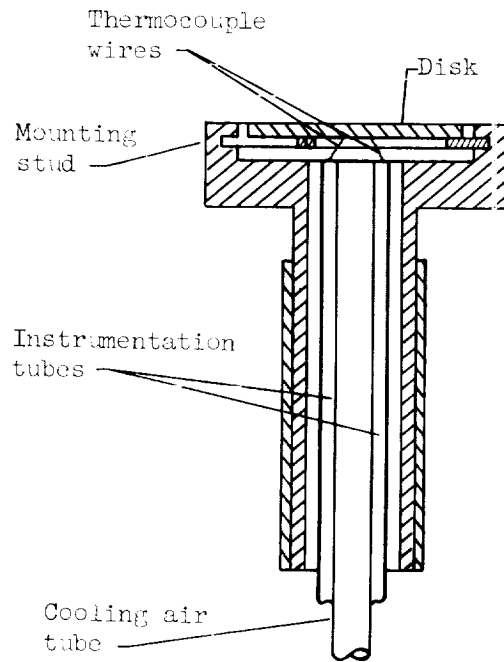
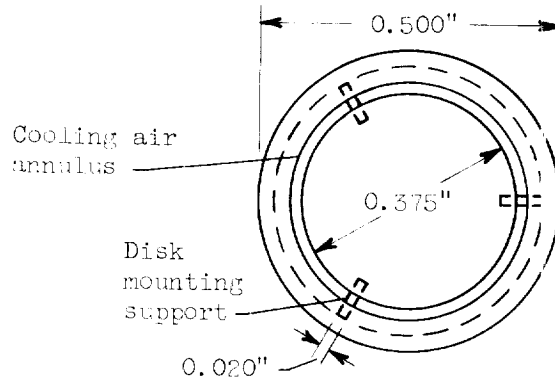


Figure 4. - Schematic illustration of model base region utilizing a nozzle for nitrogen gas injection. Nozzle spacing ratio  $D_s/D_e$ , 2.22; nozzle extension ratio  $L/D_e$ , 0.9091; configuration 6.



(a) Bayonet-type thermocouple.



(b) Disk calorimeter.

Figure 5. - Bayonet-type thermocouple and disk calorimeter.

E-1241

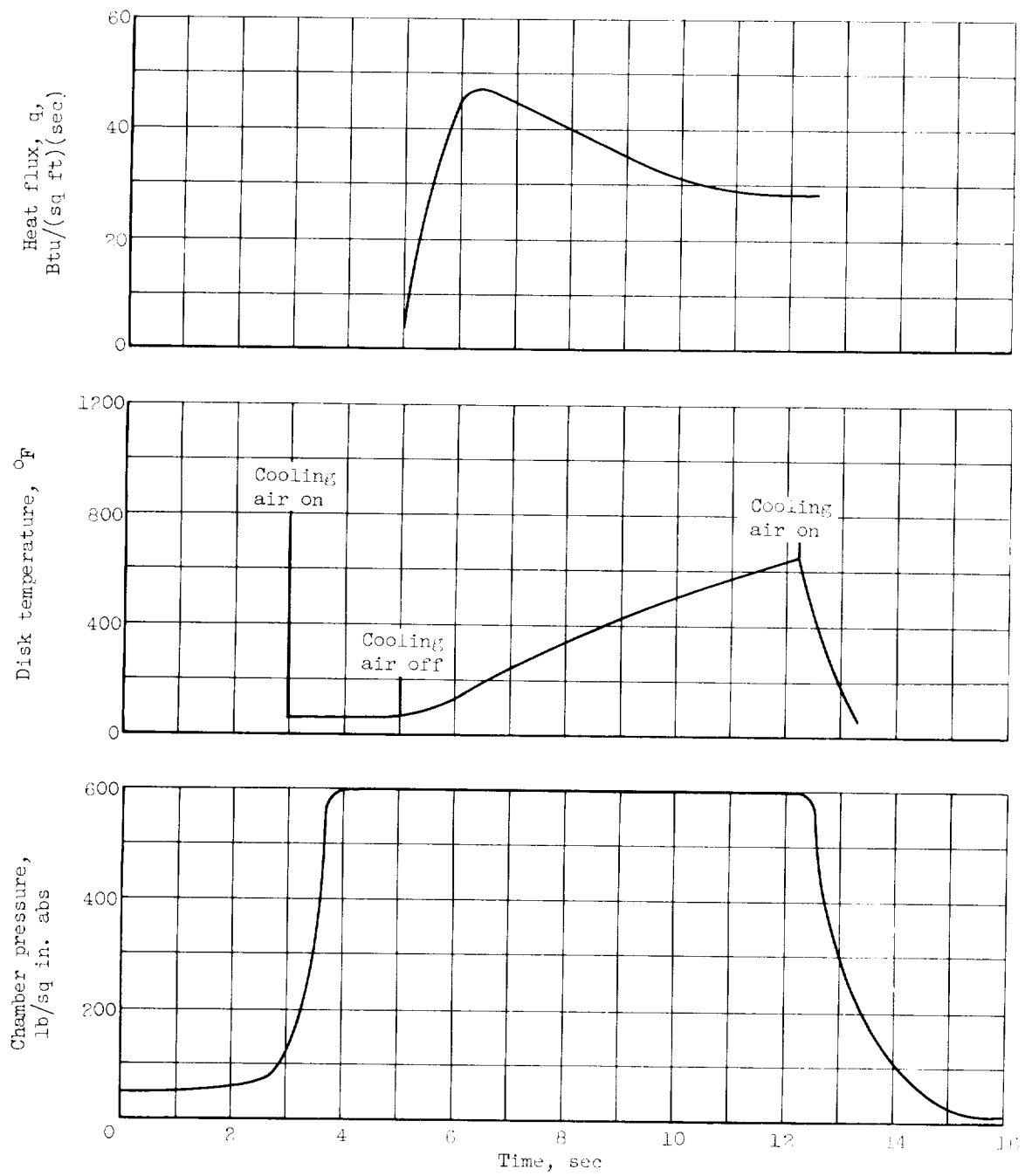
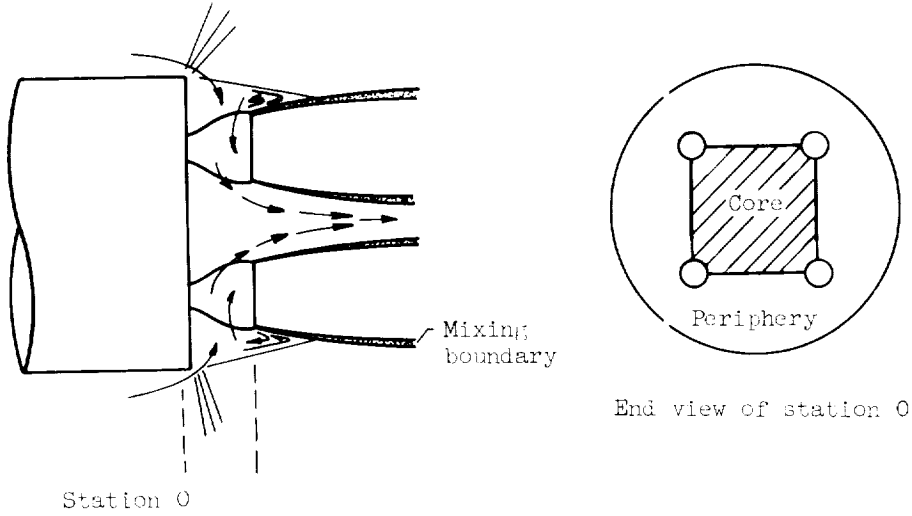
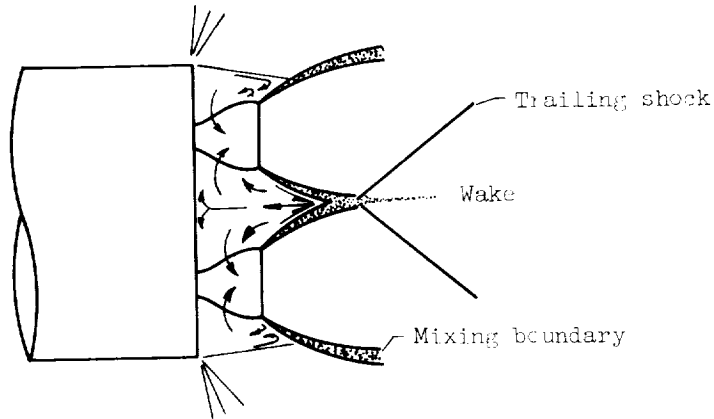


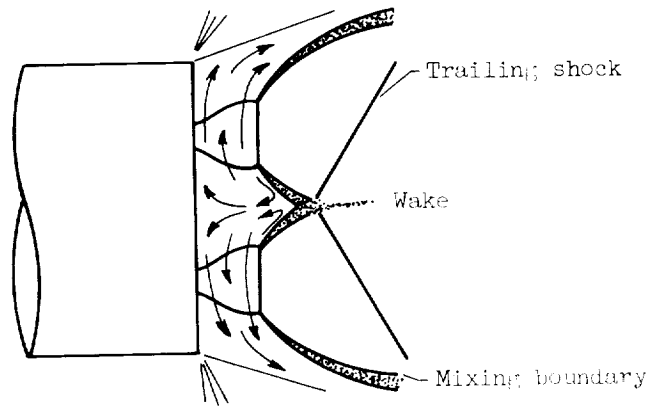
Figure 6. - Typical temperature-time history of engine chamber pressure, disk temperature, and heat flux.



(a) Aspiration flow.



(b) Transitional flow.



(c) Choked reverse flow.

Figure 7. - Base flow phenomena.

E-1241

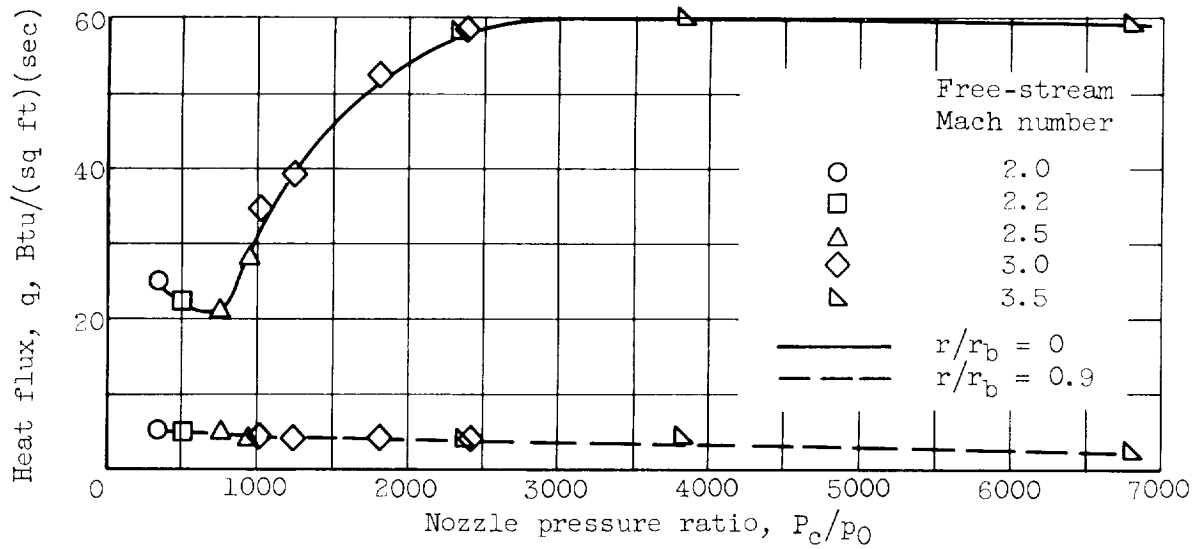
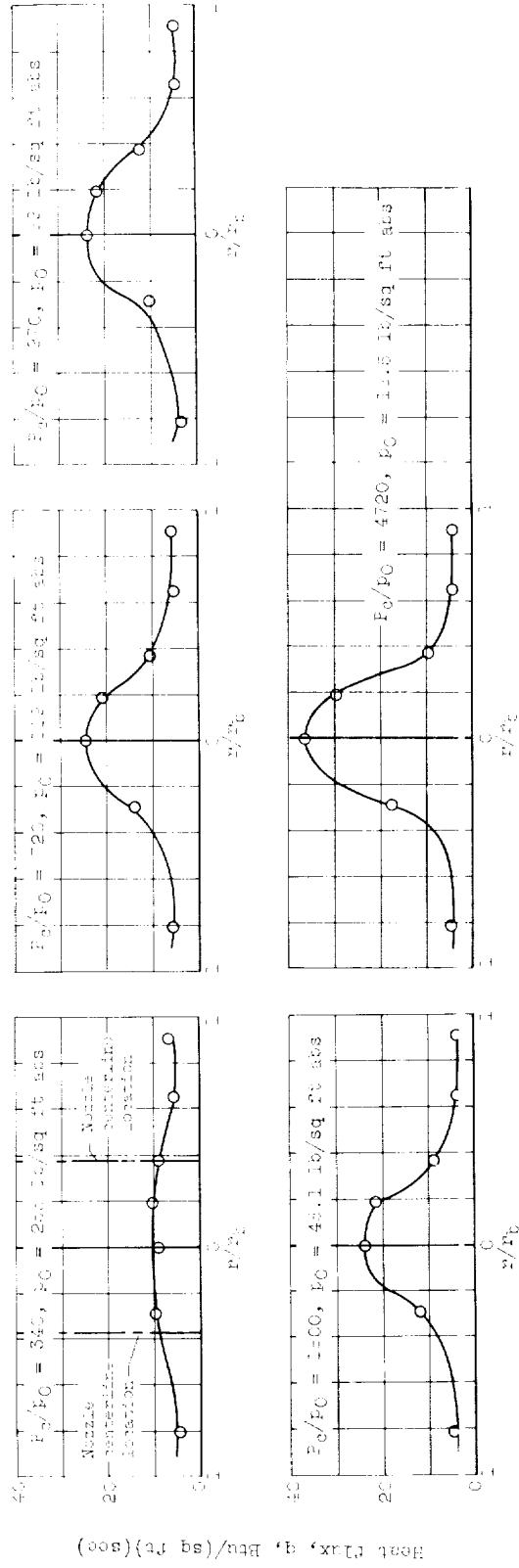
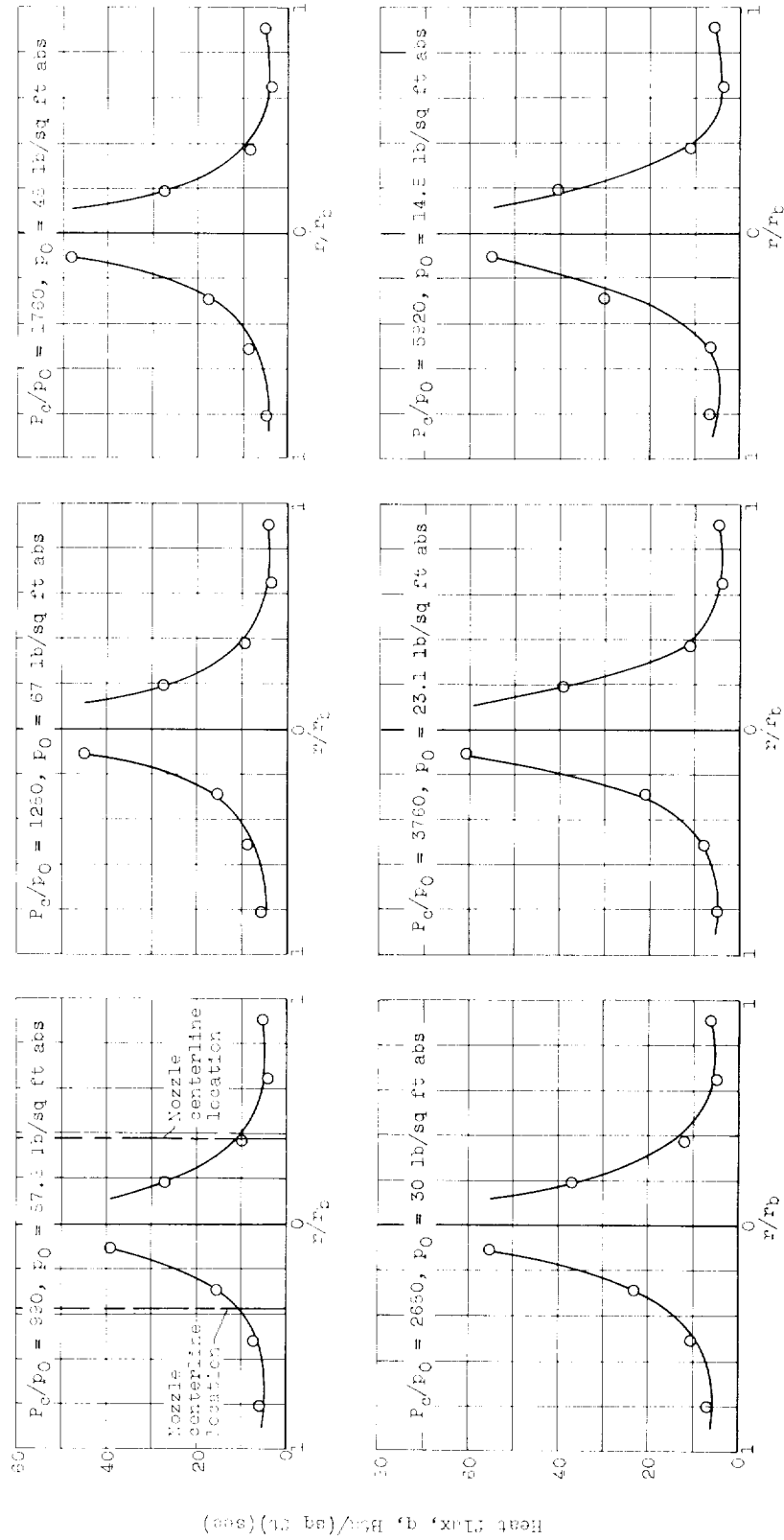


Figure 8. - Effect of free-stream Mach number on base heat flux.  
 Nozzle spacing ratio  $D_s/D_e$ , 1.67; nozzle extension ratio  
 $L/D_e$ , 1.5306; configuration 2.

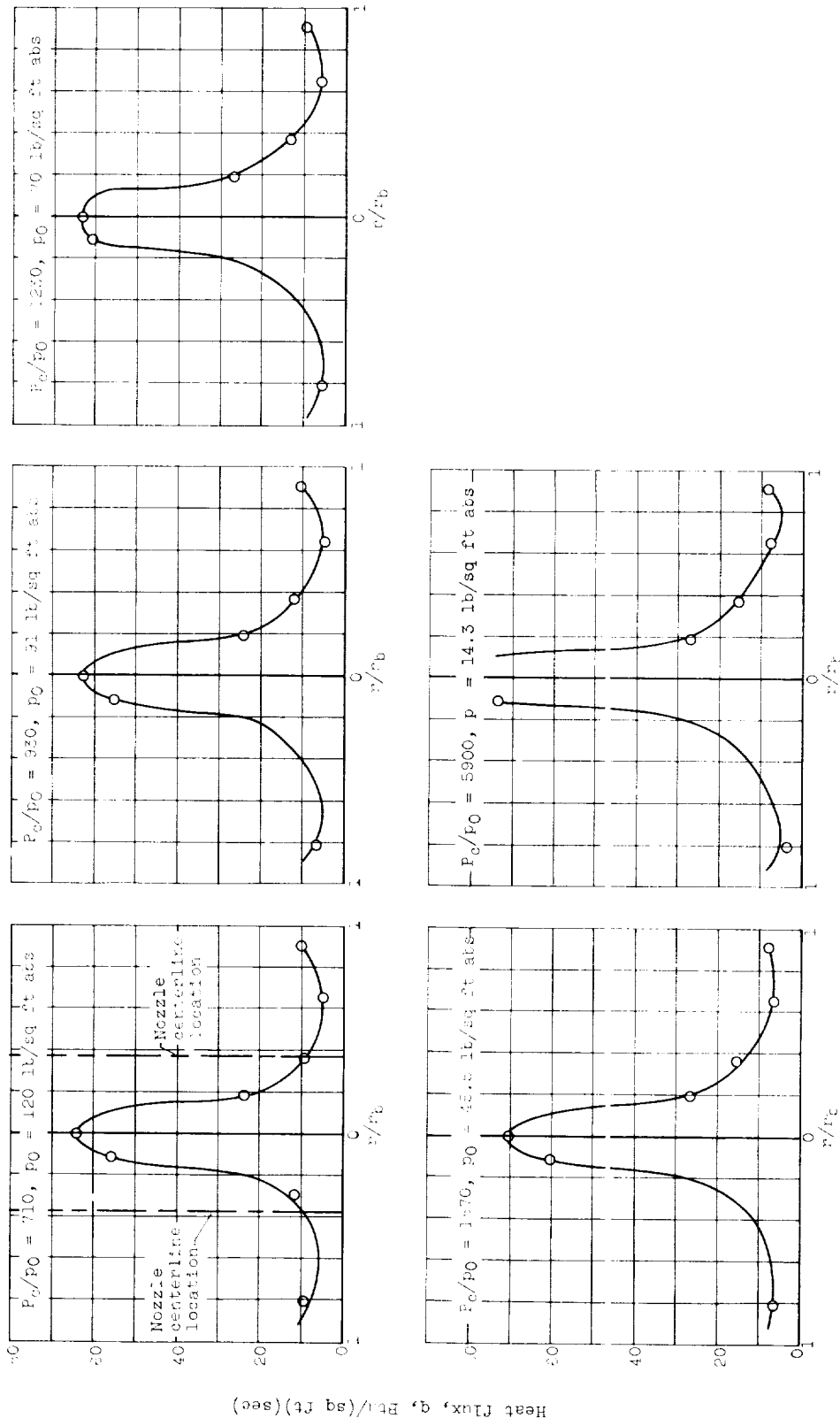


(a) Configuration in; nozzle expansion ratio  $L/D_0 = 1.7326$ .  
 Figure 3. - Effect of nozzle pressure ratio on base heat flux distribution for a nozzle spacing ratio  $D_0/D_c$  of 2.11.



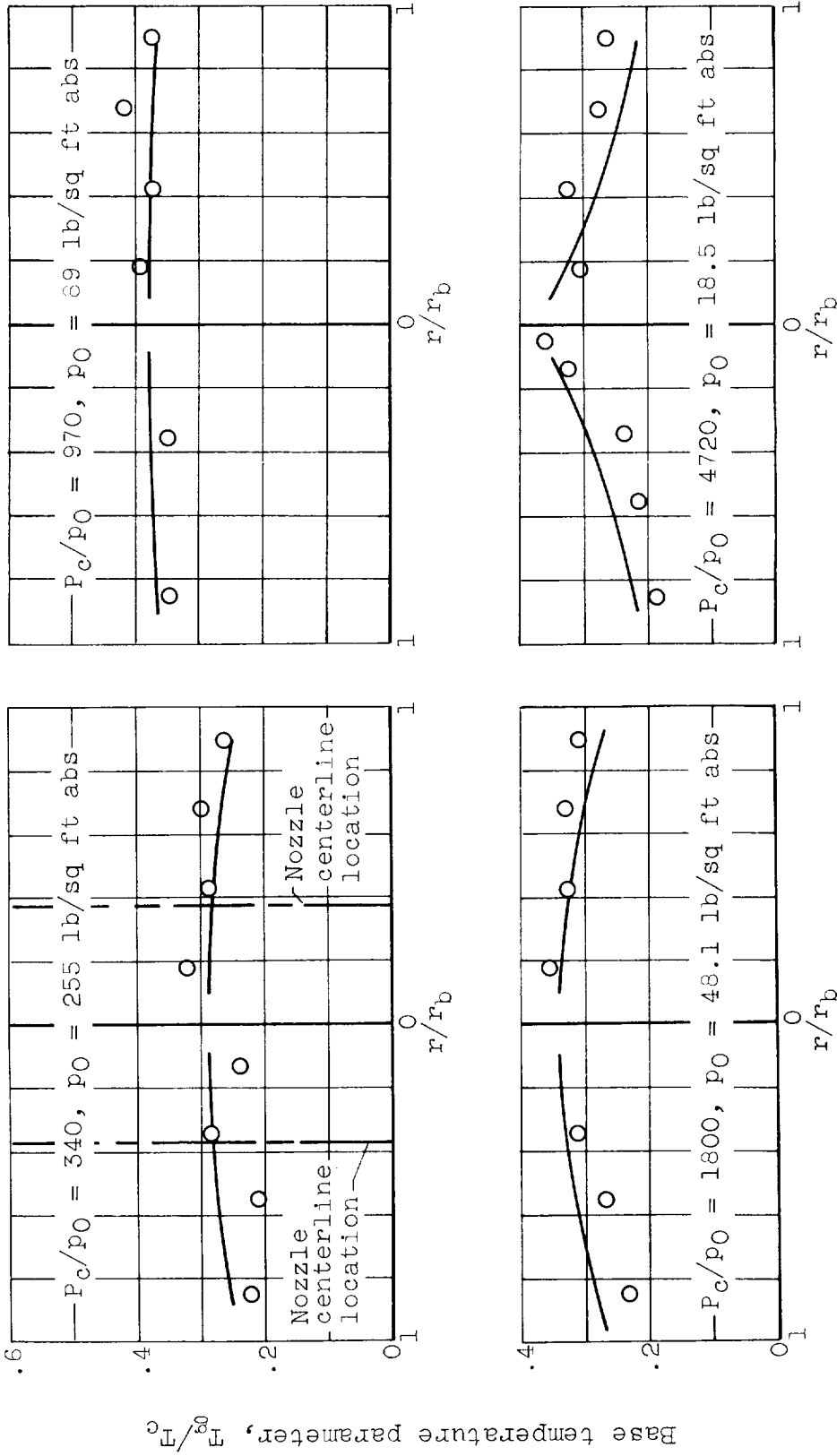
(b) Configuration 1b; nozzle extensior ratio  $L/D_e, 0.701b$ .

Figure 2. - Continued. Effect of nozzle pressure ratio on base heat flux distribution for a nozzle spacing ratio  $D_s/D_e$  of 2.18.



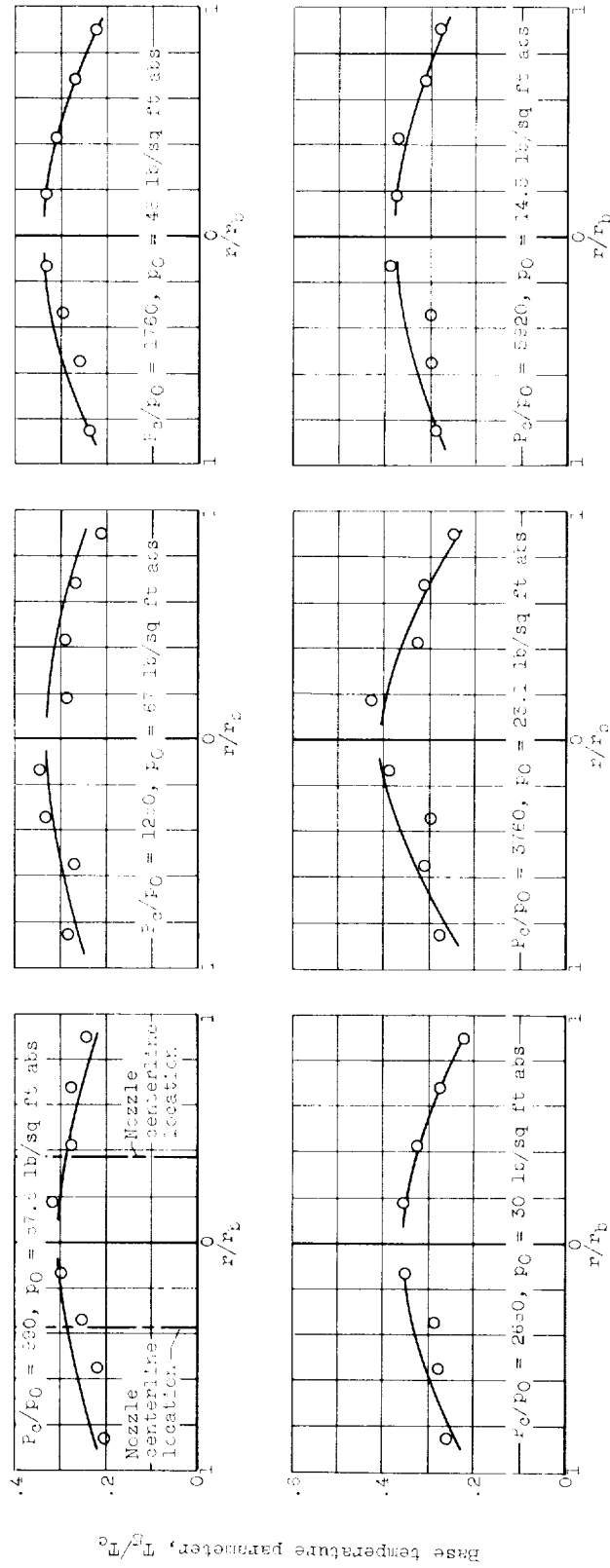
(c) Configuration 1c; nozzle extension ratio  $l/D_0$ , 0.0425.

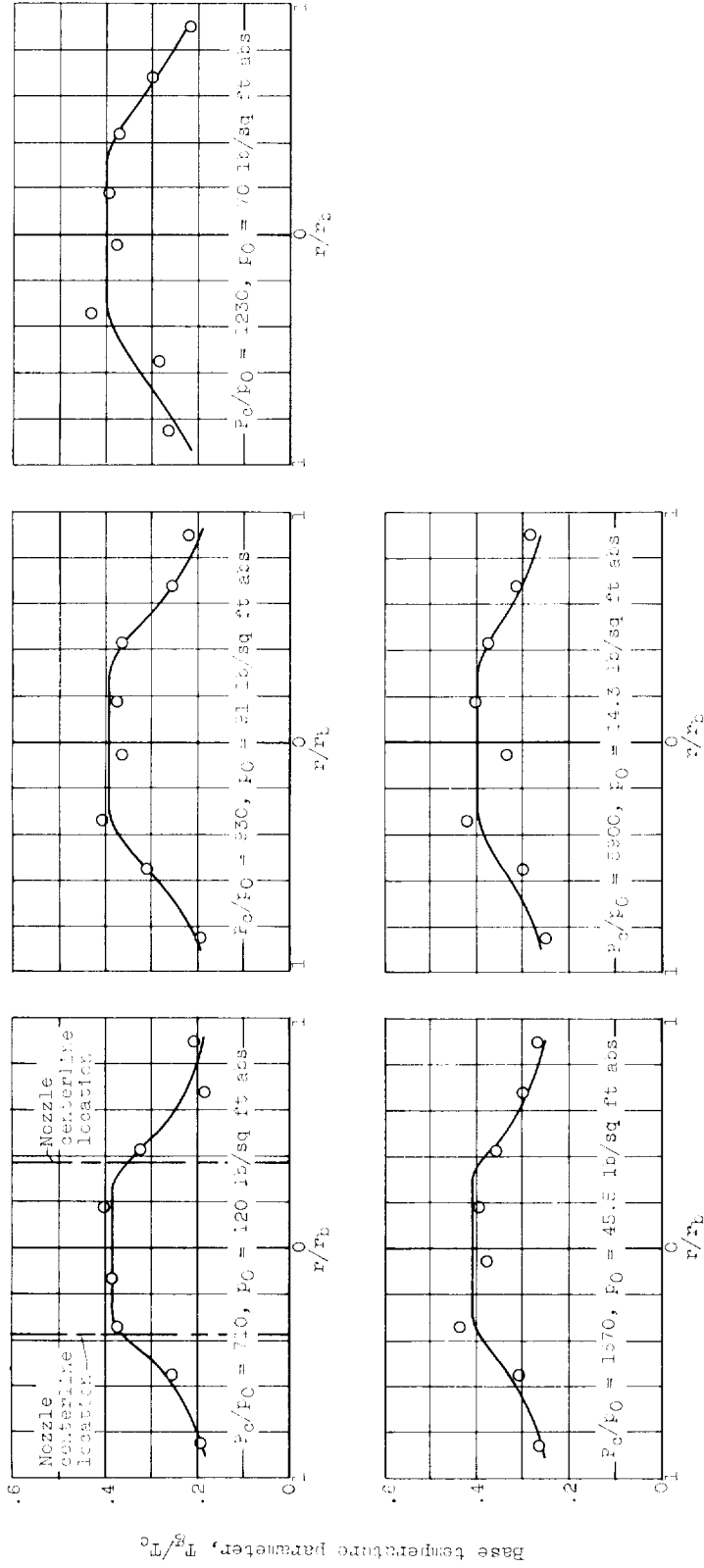
Figure 9. - Concluded. Effect of nozzle pressure ratio on base heat flux distribution for a nozzle speed ratio  $D_0/D_0^*$  of 2.1c.



(a) Configuration 1a; nozzle extension ratio  $L/D_e$ , 1.7326.

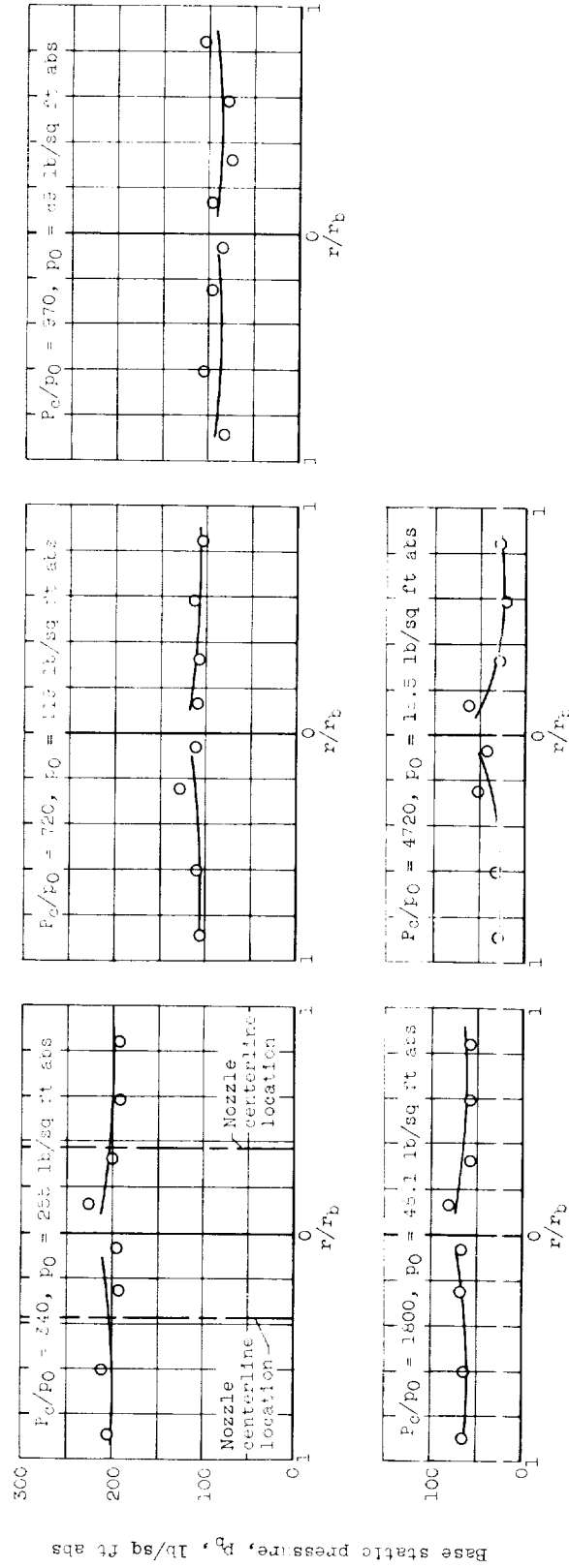
Figure 10. - Effect of nozzle pressure ratio on base temperature parameter distribution for a nozzle spacing ratio  $D_s/D_e$  of 2.15.



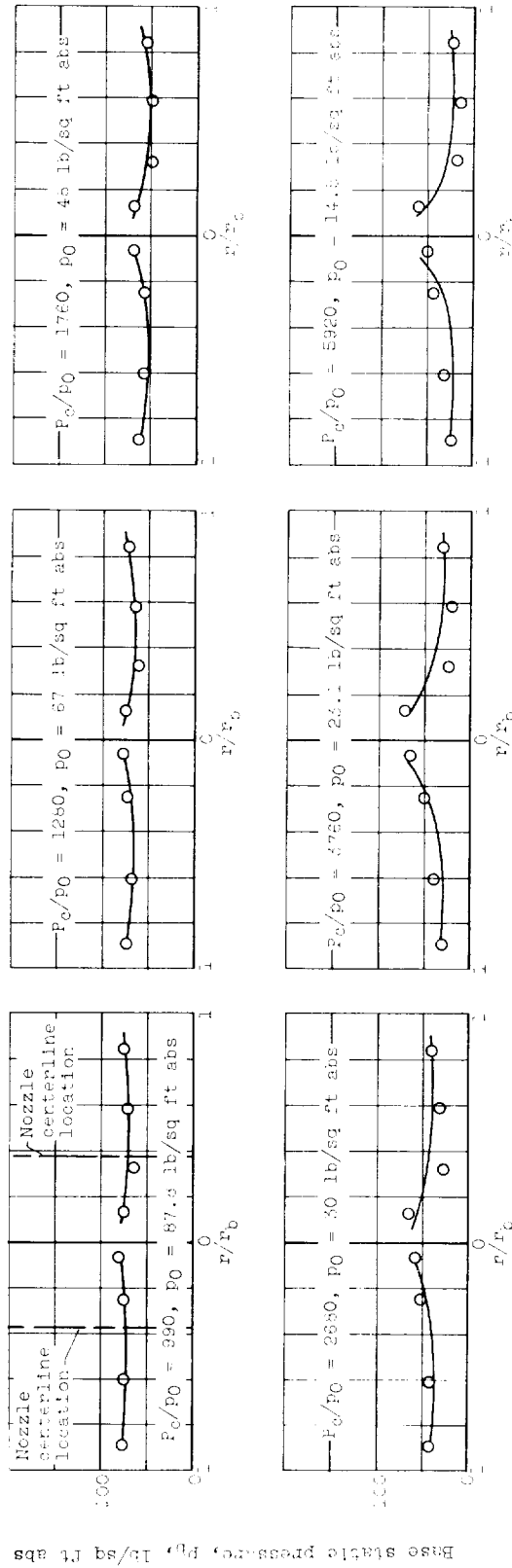


(a) Configuration 1a; nozzle extension ratio  $L/D_0, 0.0425$ .

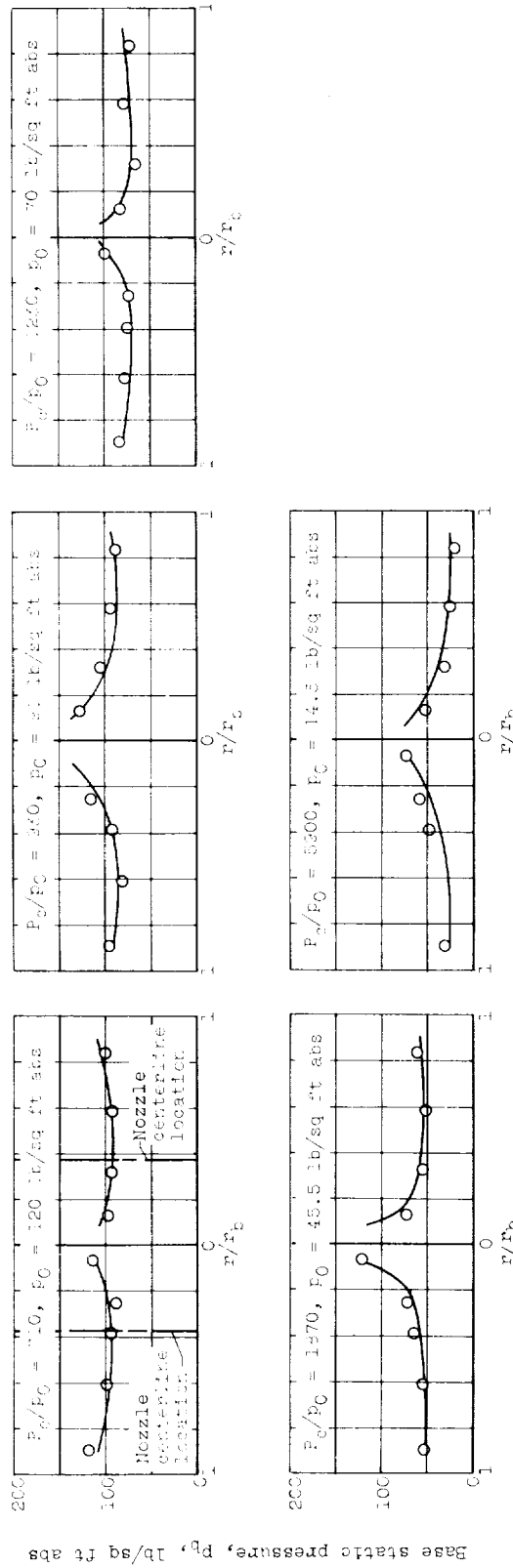
Figure 10. - Concluded. Effect of nozzle pressure ratio on base temperature parameter distribution for a nozzle spudlet ratio  $D_g/D_e$  of 2.15.



(a) Configuration 1a; nozzle extension ratio  $L/D_e$ , 1.7326.  
 Figure 11. - Effect of nozzle pressure ratio on base pressure distribution for a nozzle spacing ratio  $D_g/D_e$  of 2.18.



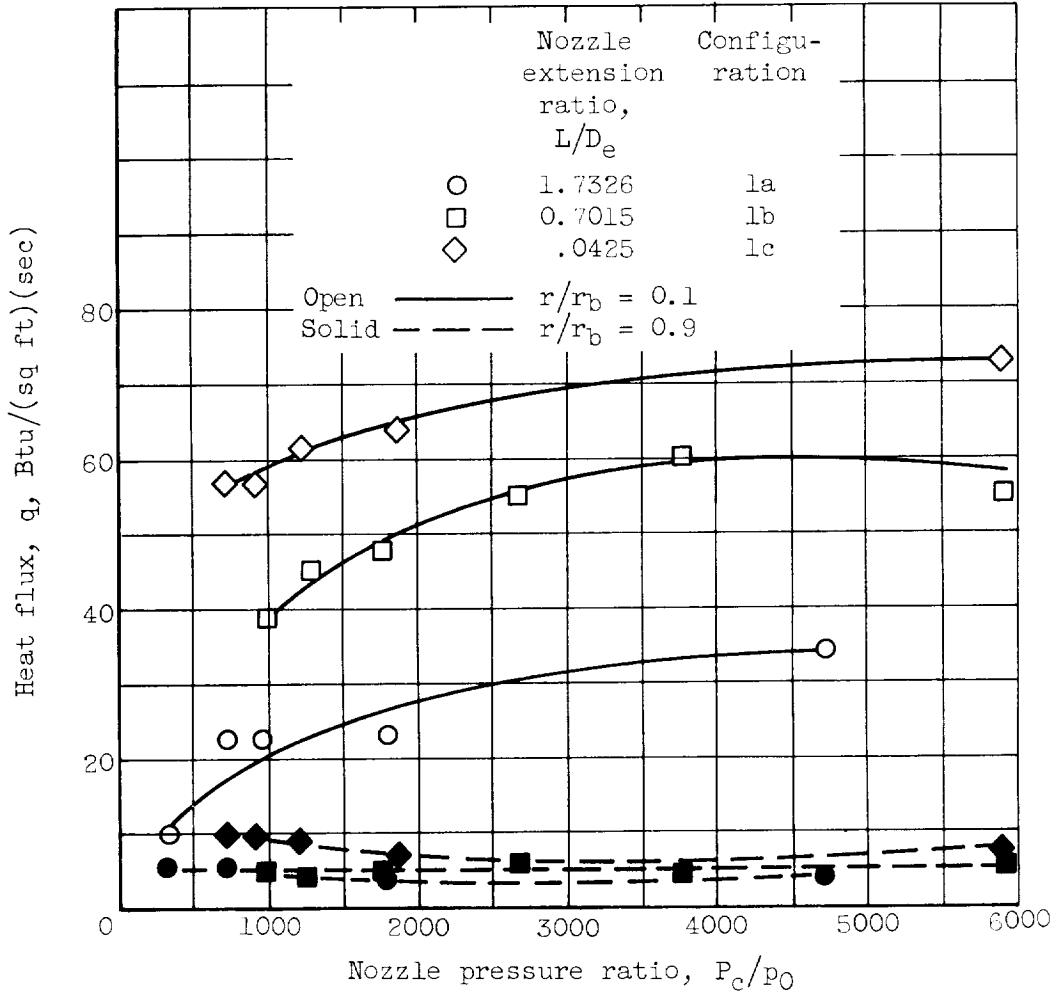
(b) Configuration 1b; nozzle extension ratio  $L/D_n = 0.701r$ .  
 Effect of nozzle pressure ratio on base pressure distribution for a nozzle spacing ratio  $D_s/D_n$  of 2.15.



(c) Configuration 1e; nozzle extension ratio  $L/D_e$ , 0.0425.

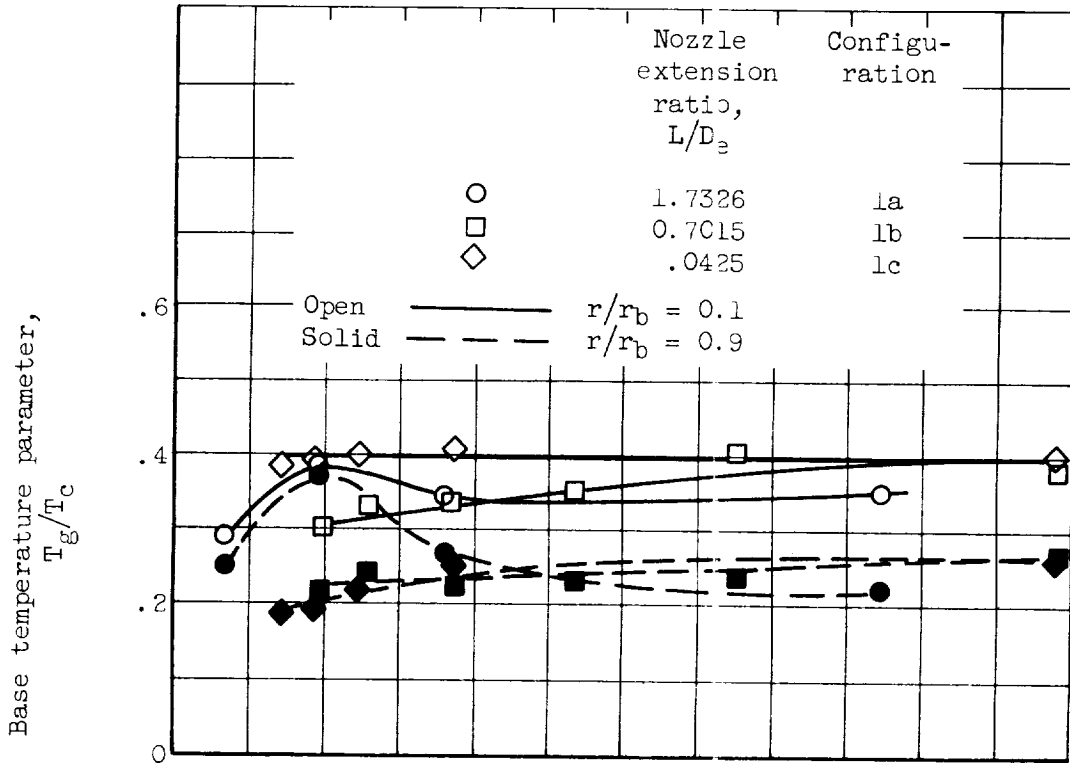
Figure 11. - Concluded. Effect of nozzle pressure ratio or base pressure distribution for a nozzle spacing ratio  $D_s/D_e$  of 2.16.

E-1241

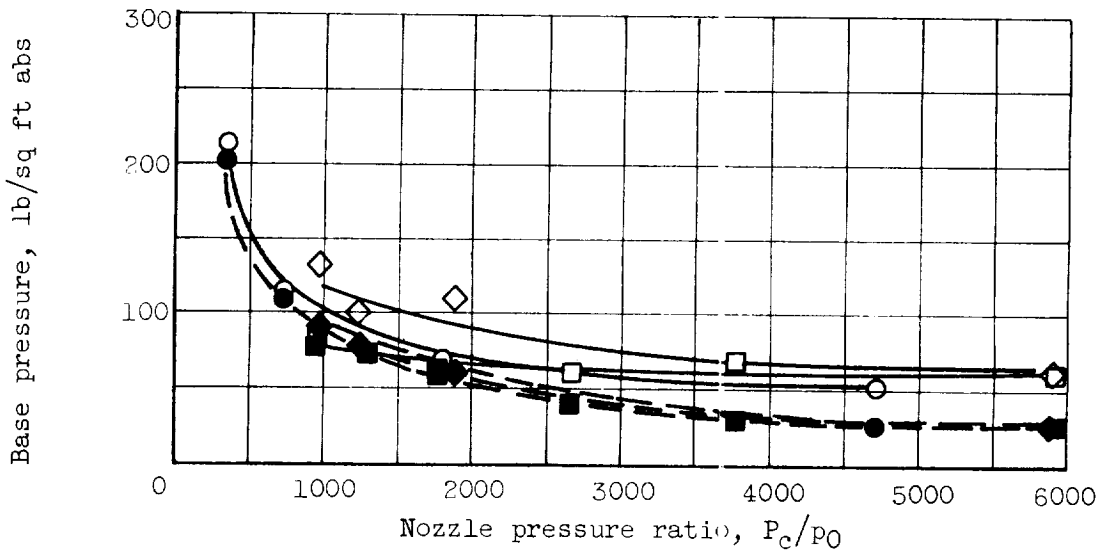


(a) Heat flux.

Figure 12. - Effect of rocket nozzle extension on model base parameters.

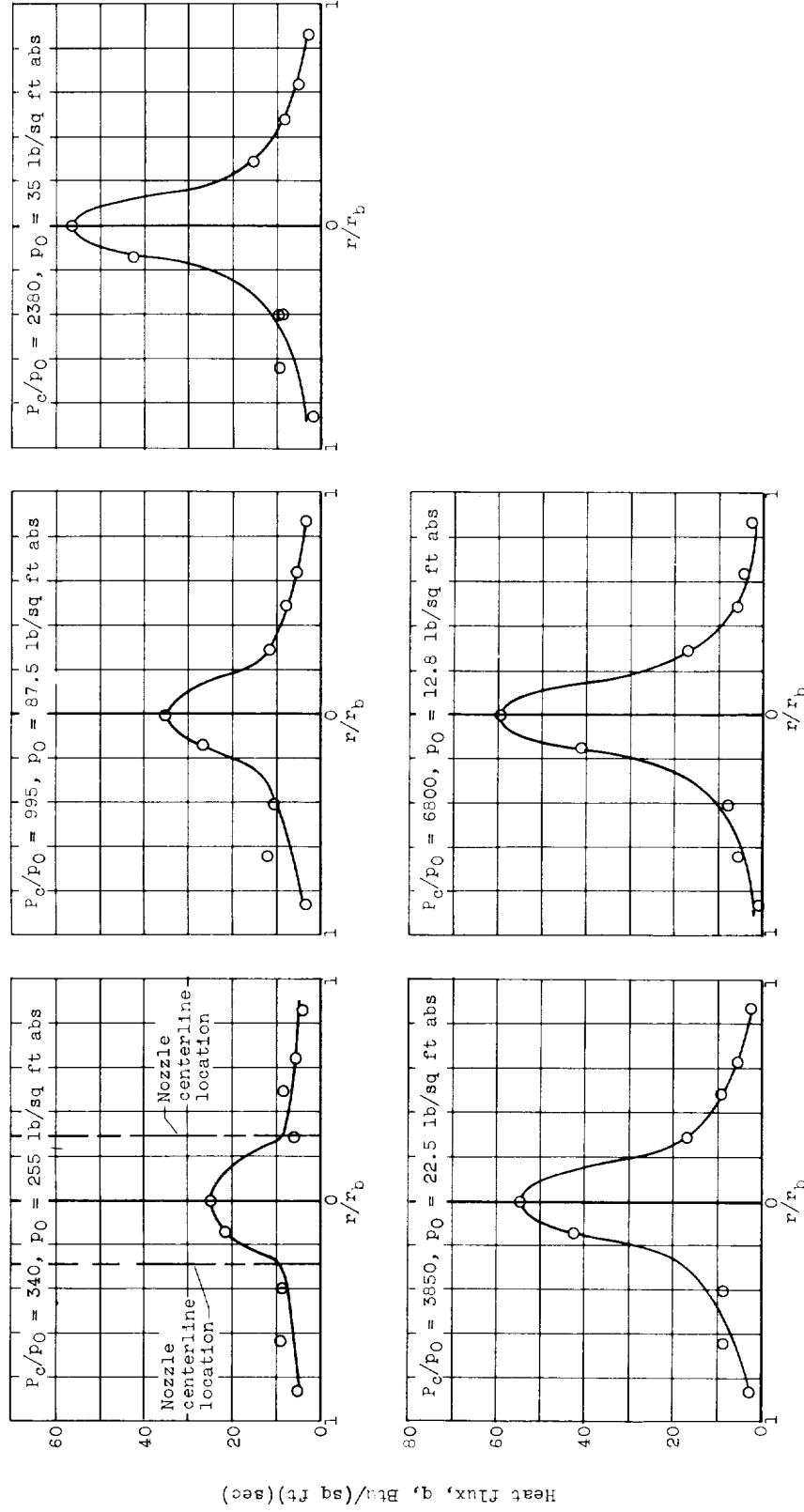


(b) Base temperature parameter.



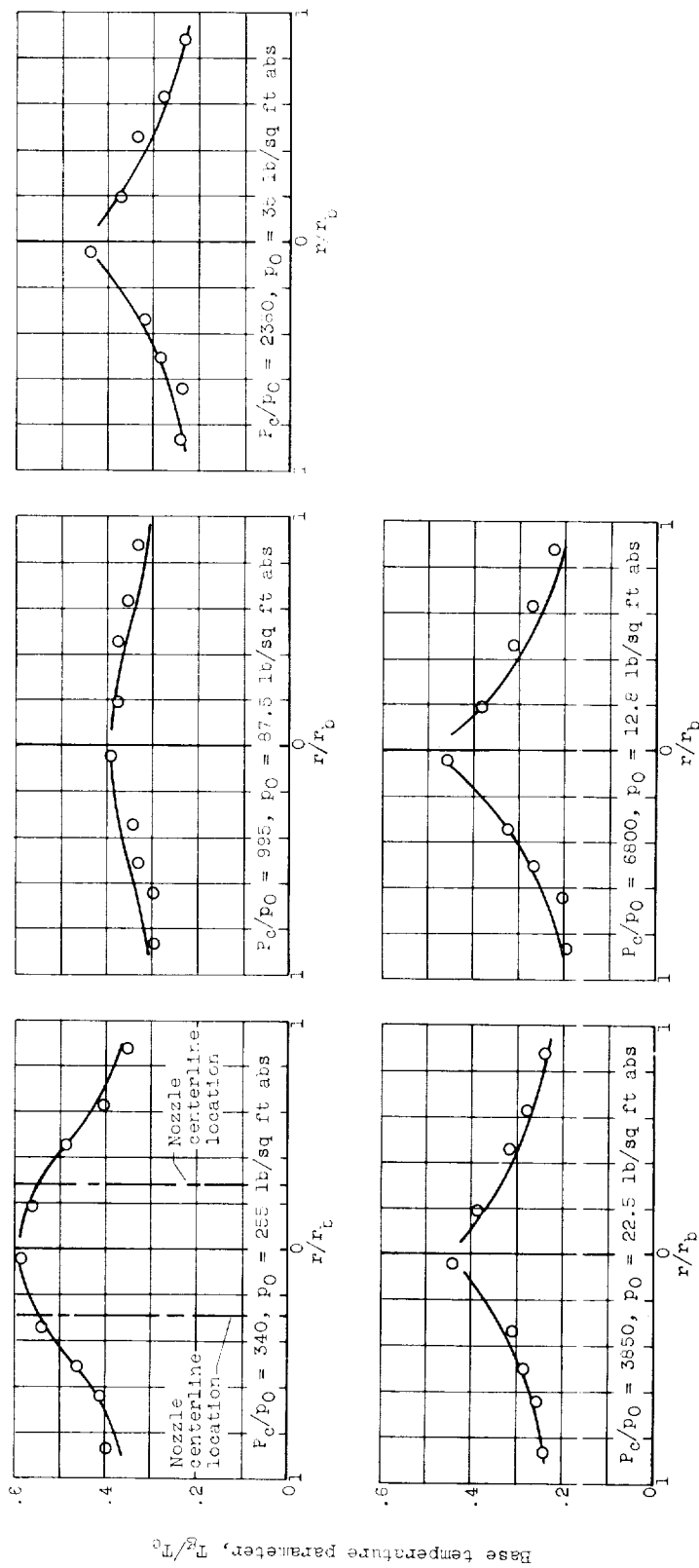
(c) Base pressure.

Figure 12. - Concluded. Effect of rocket nozzle extension on model base parameters.



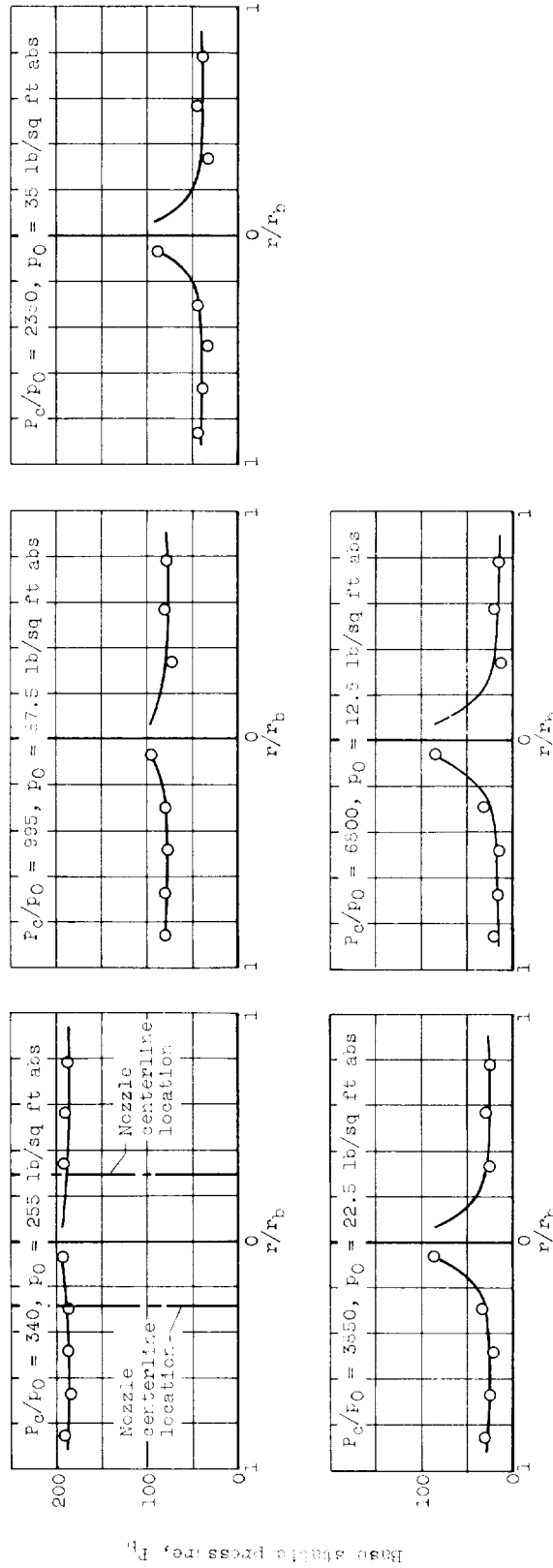
(a) Base heat flux distribution.

Figure 13. - Effect of nozzle pressure ratio on model base parameters for a nozzle spacing ratio  $D_g/D_e$  of 1.67 and an extension ratio  $L/D_e$  of 1.5306; configuration 2.



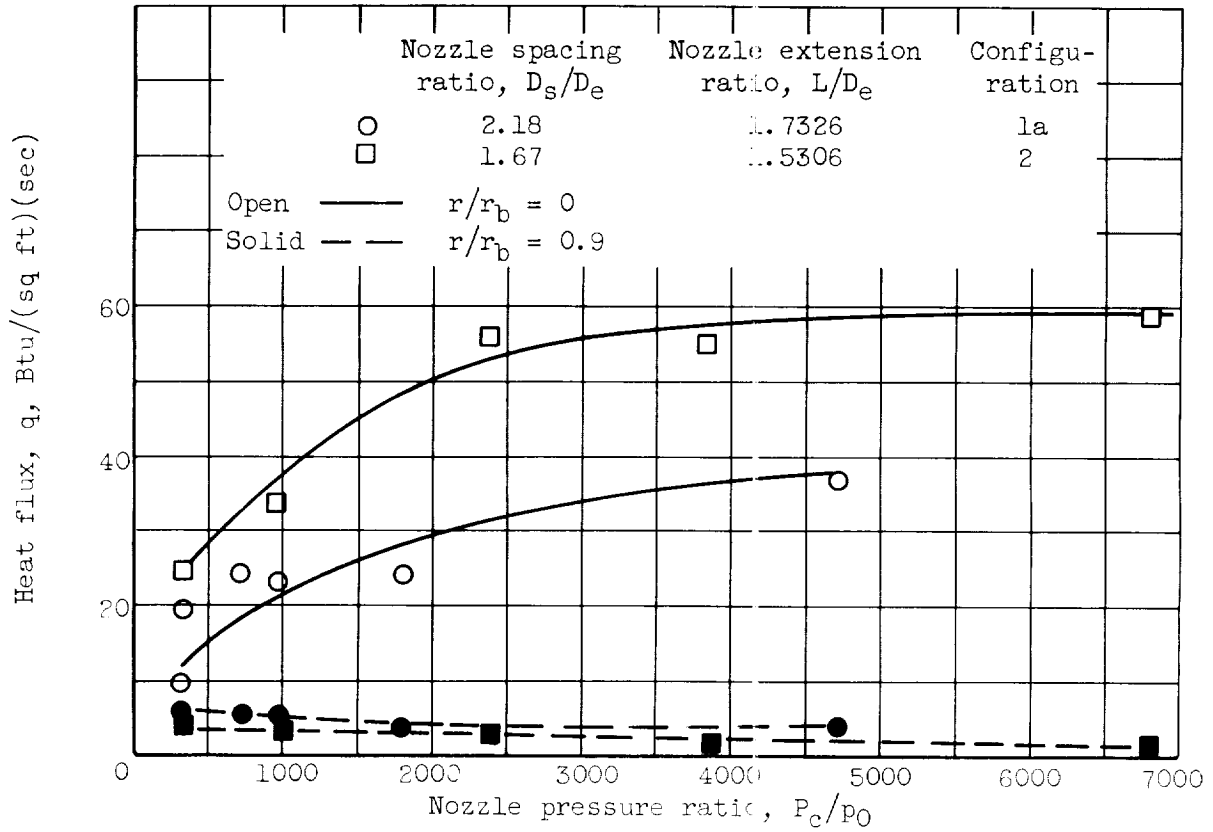
(b) Base temperature parameter distribution.

Figure 13. - Continued. Effect of nozzle pressure ratio on model base parameters for a nozzle spacing ratio  $D_s/D_e$  of 1.67 and an extension ratio  $L/D_e$  of 1.5306; configuration 2.



(c) Base pressure distribution.

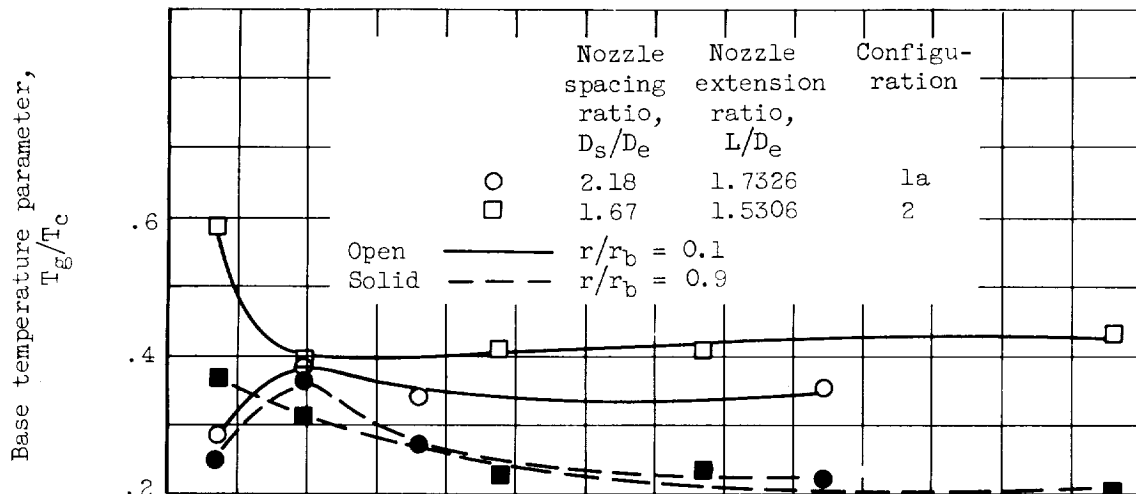
Figure 13. - Concluded. Effect of nozzle pressure ratio on model base parameters for a nozzle spacing ratio  $D_s/D_e$  of 1.67 and an extension ratio  $L/D_e$  of 1.506; configuration 2.



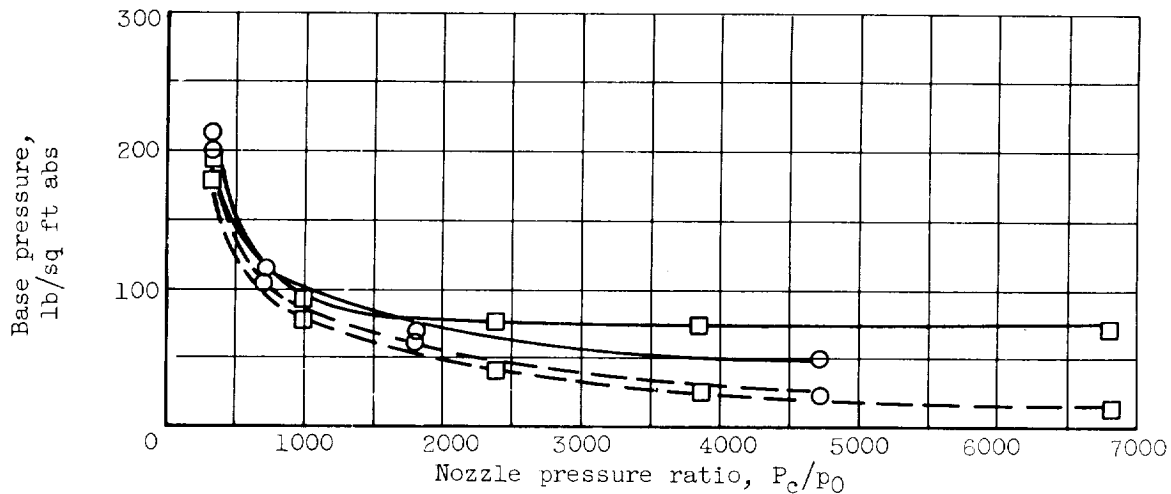
(a) Heat flux.

Figure 14. - Effect of decreasing nozzle spacing ratio on model base parameters.

E-1241

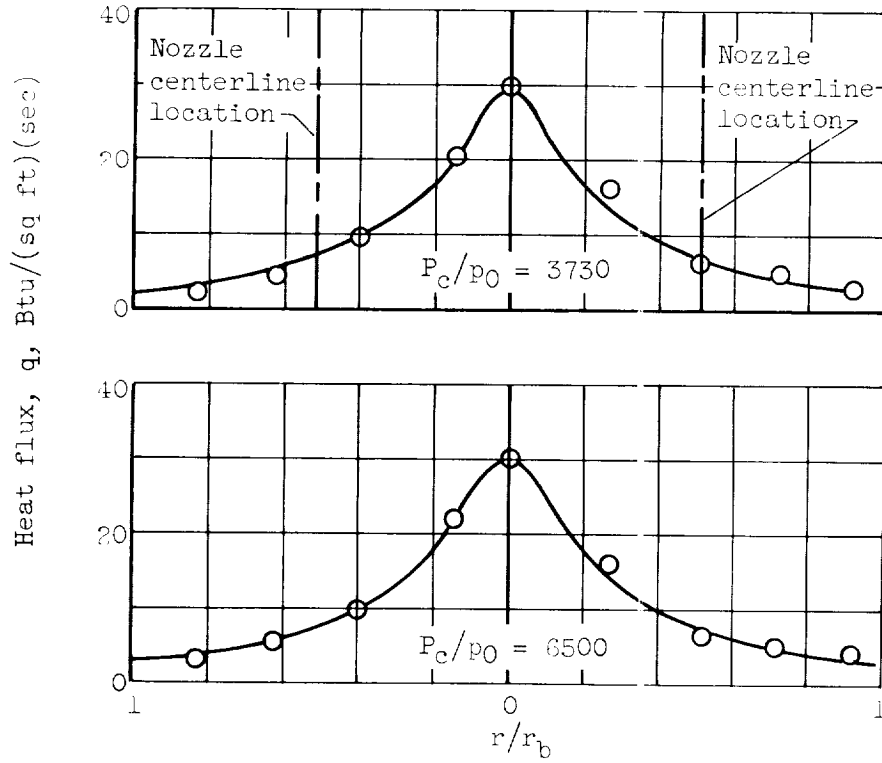


(b) Base temperature parameter.



(c) Base pressure.

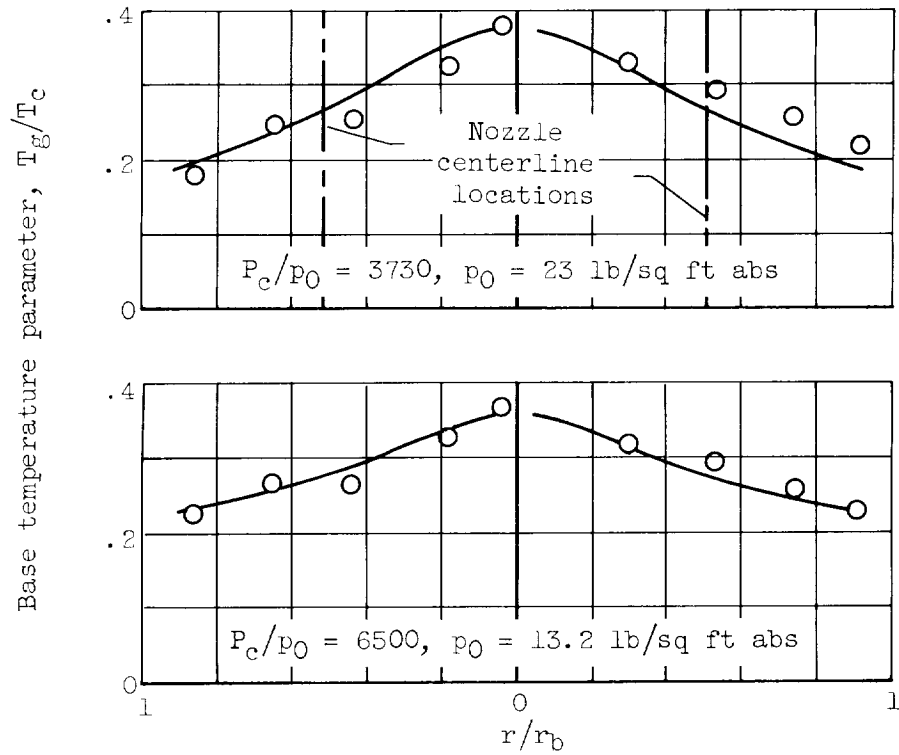
Figure 14. - Concluded. Effect of decreasing nozzle spacing ratio on model base parameters.



(a) Base heat flux distribution.

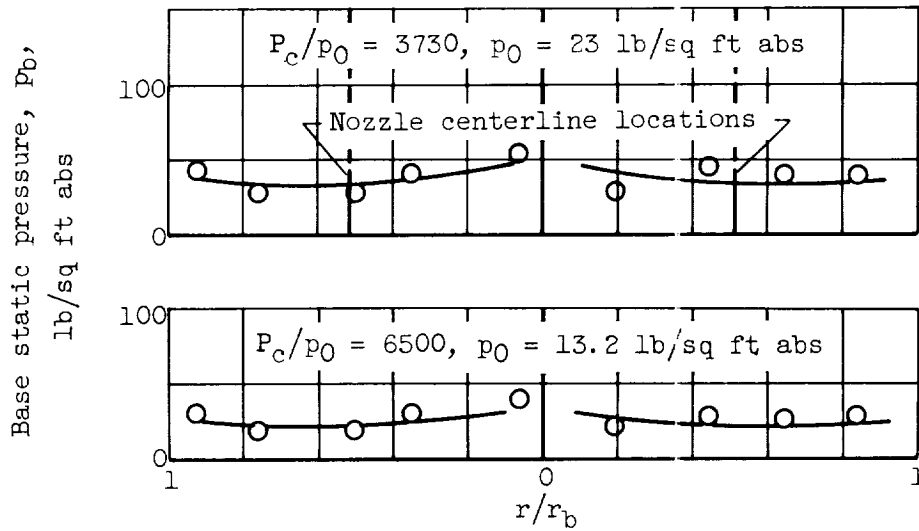
Figure 15. - Effect of nozzle pressure ratio on model base parameters for a nozzle spacing ratio  $D_s/D_e$  of 2.97 and a nozzle extension ratio  $L/D_e$  of 0.6803; configuration 3.

E-1241



(b) Base temperature parameter distribution.

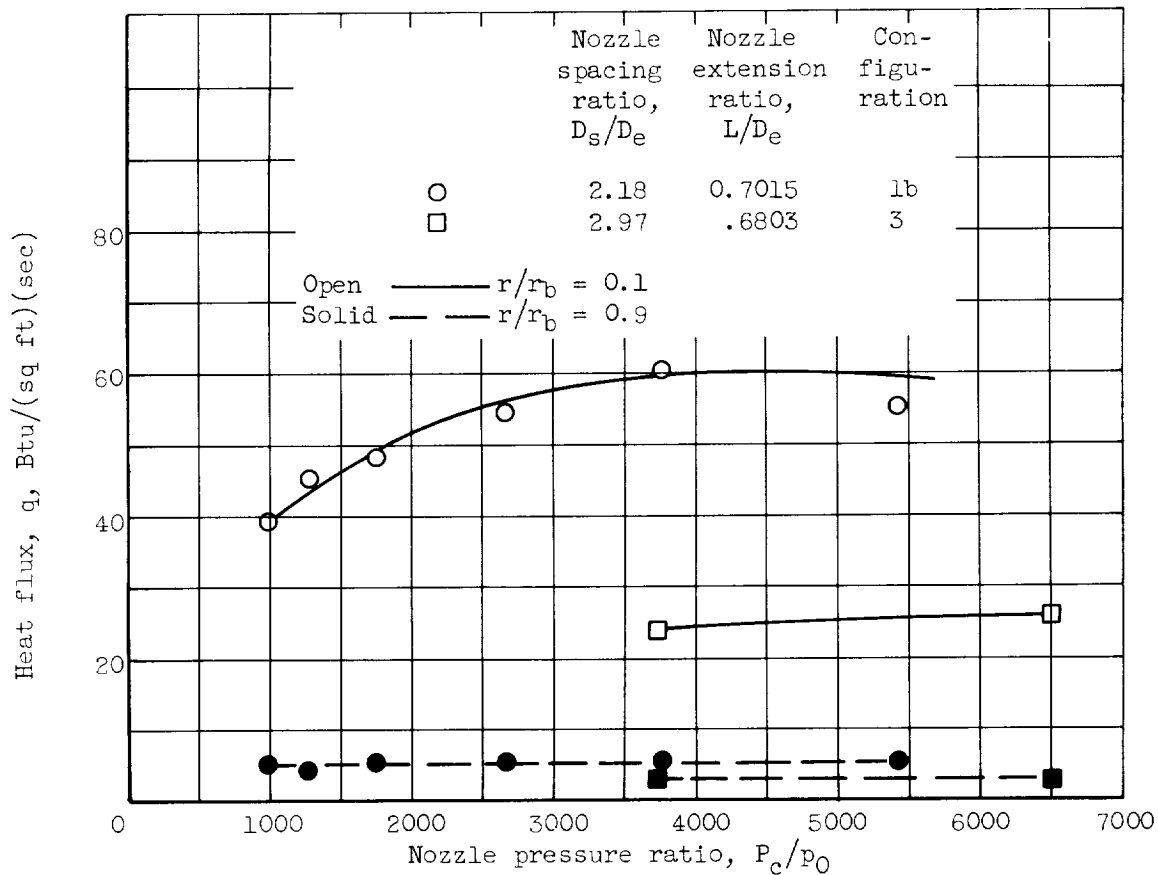
Figure 15. - Continued. Effect of nozzle pressure ratio on model base parameters for a nozzle spacing ratio  $D_s/D_e$  of 2.97 and a nozzle extension ratio  $L/D_e$  of 0.6803; configuration 3.



(c) Base pressure distribution.

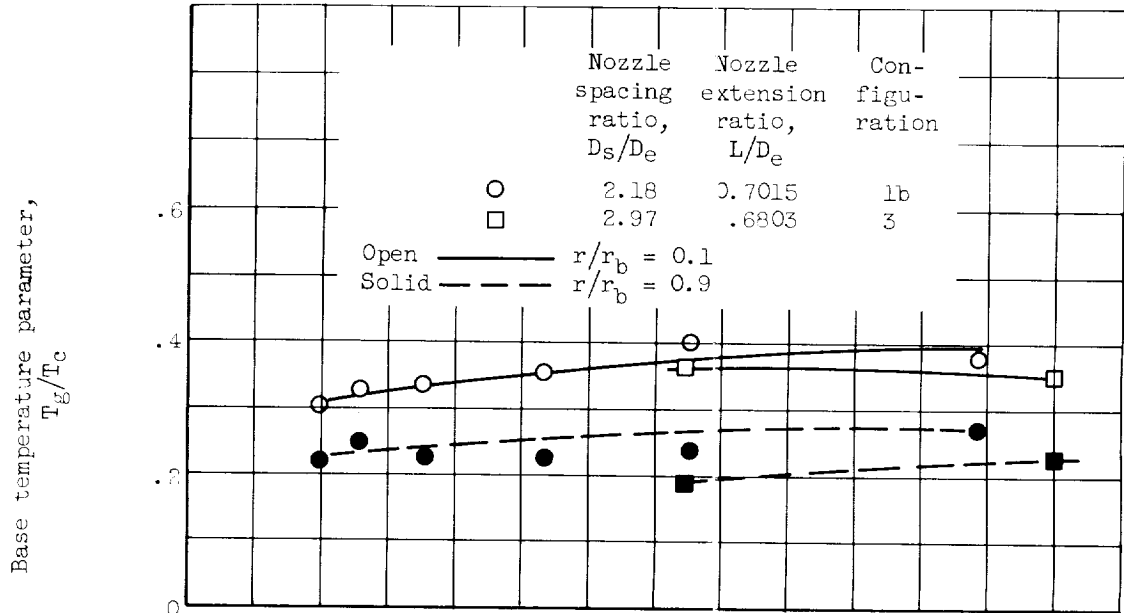
Figure 15. - Concluded. Effect of nozzle pressure ratio on model base parameters for a nozzle spacing ratio  $D_s/D_e$  of 2.97 and a nozzle extension ratio  $L/D_e$  of 0.6803; configuration 3.

E-1241

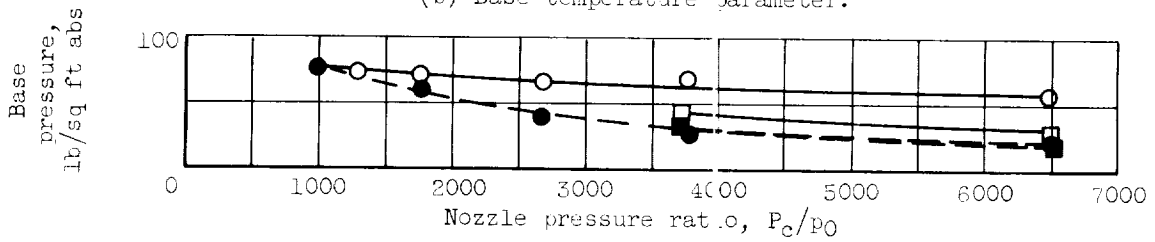


(a) Heat flux.

Figure 16. - Effect of increasing nozzle spacing ratio on model base parameters.

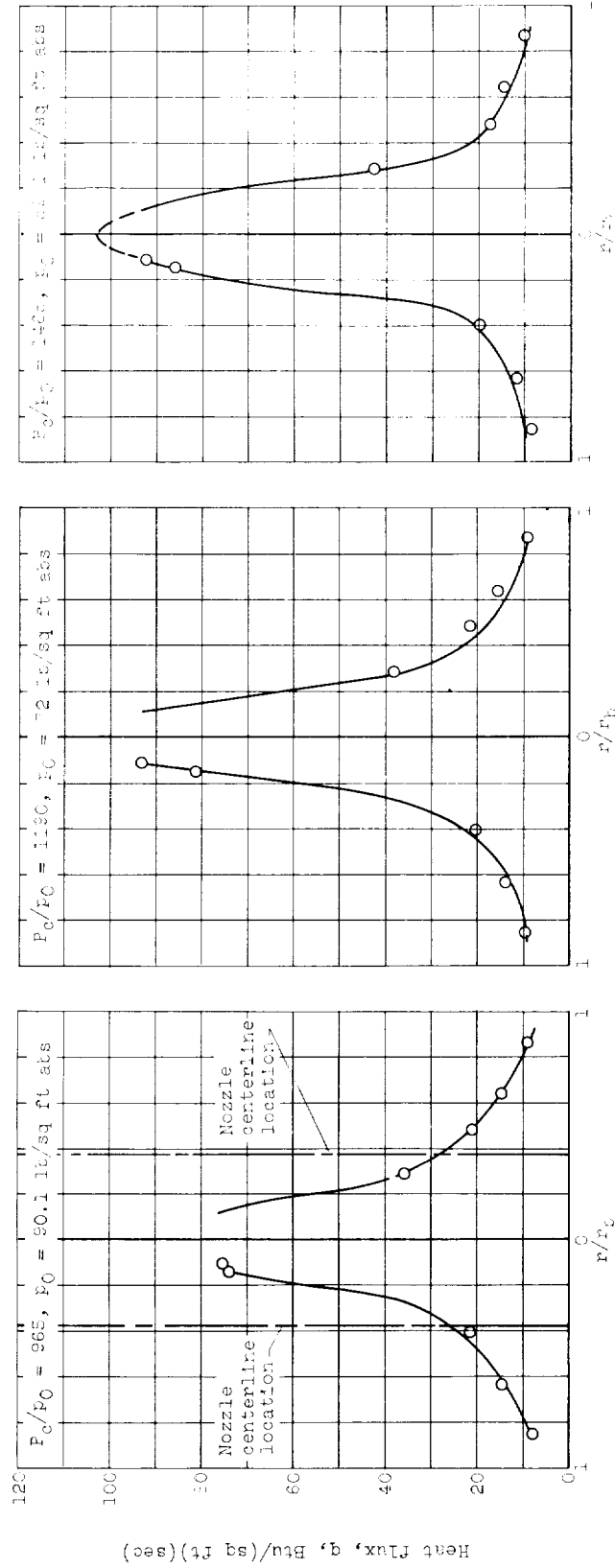


(b) Base temperature parameter.



(c) Base pressure.

Figure 16. - Concluded. Effect of increasing nozzle spacing ratio on model base parameters.



(a) Base heat flux distribution.

Figure 17. - Effect of nozzle pressure ratio on model case parameters. Conical nozzles; spacing ratio  $D_0/D_0$ , 2.22; nozzle extension ratio  $L/D_0$ , 0.8081; configuration 4.

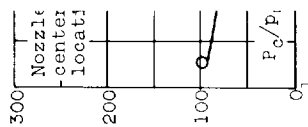


Figure 2.22

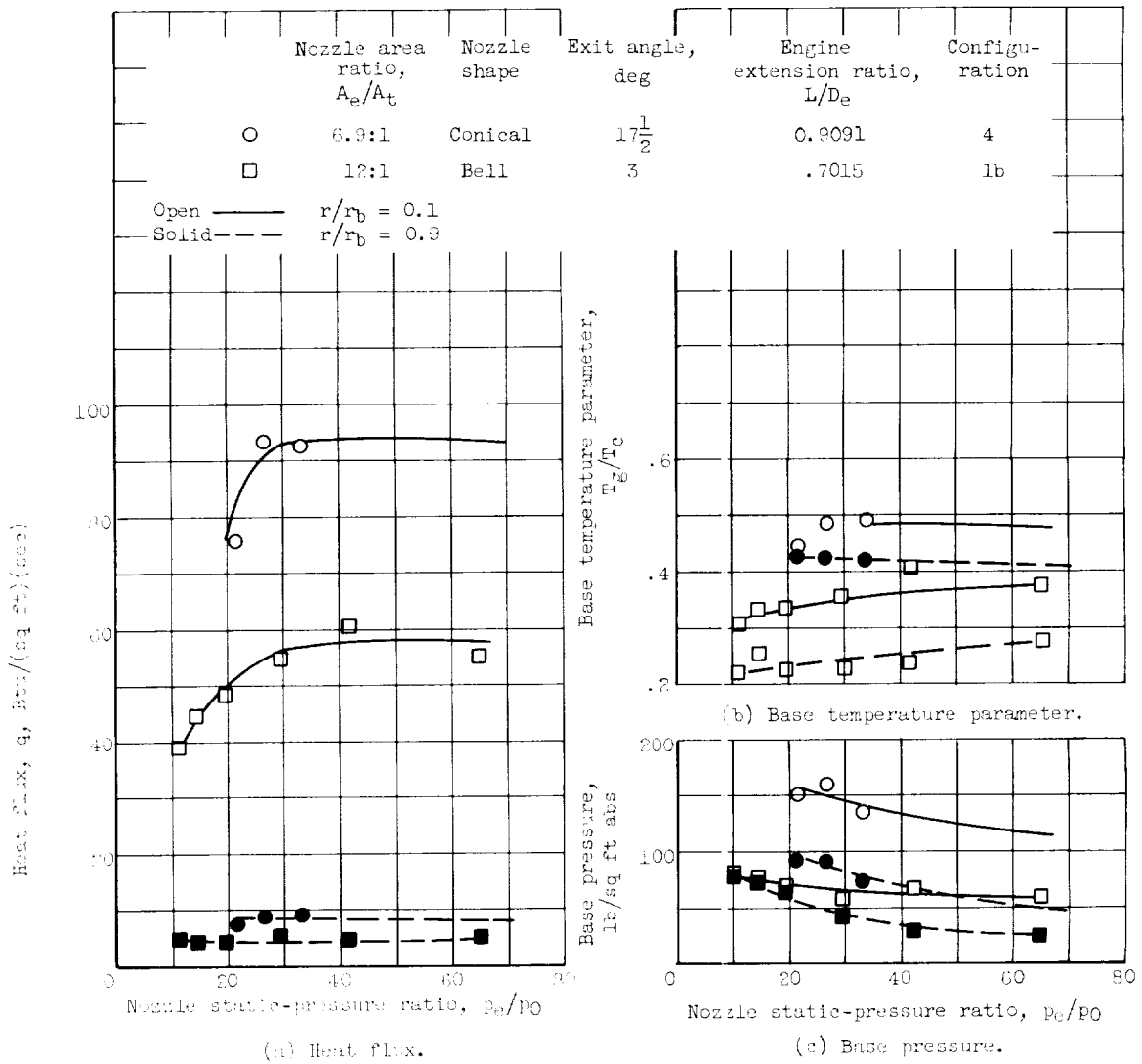
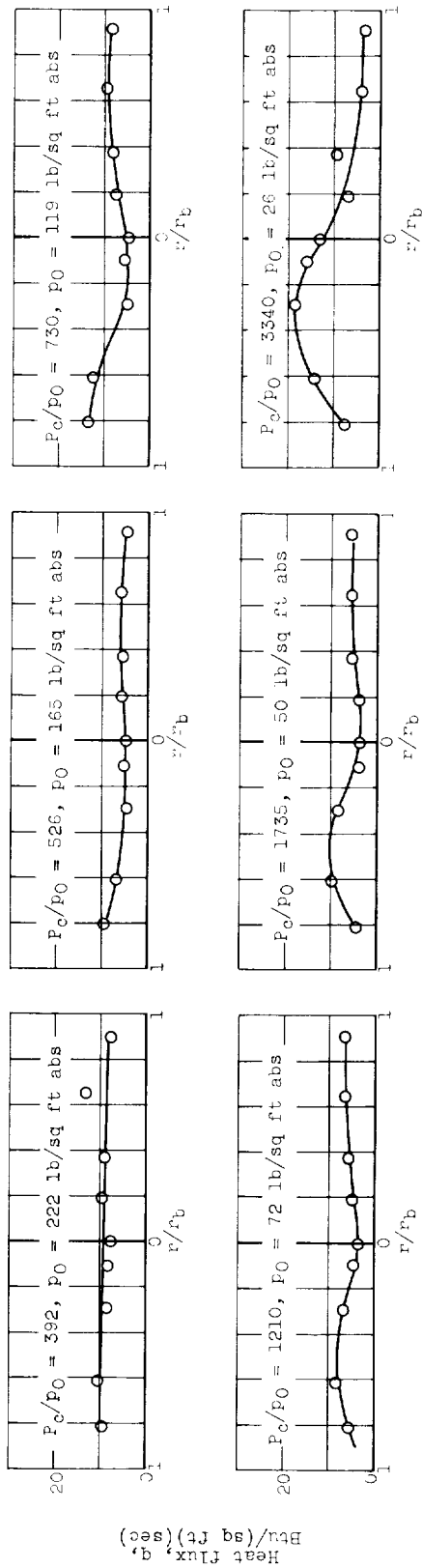
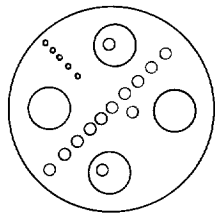
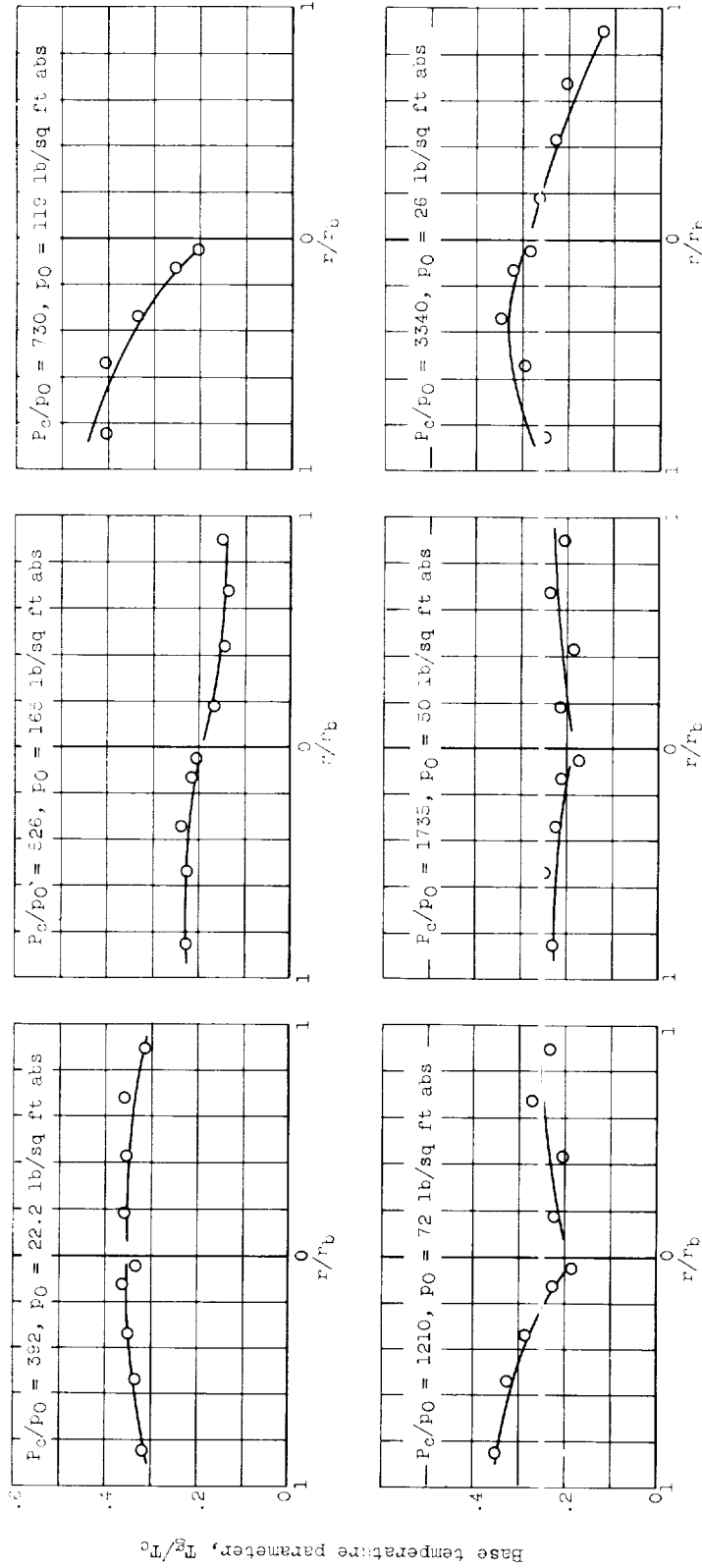


Figure 18. - Effect of nozzle area ratio and exit angle on model base parameters.

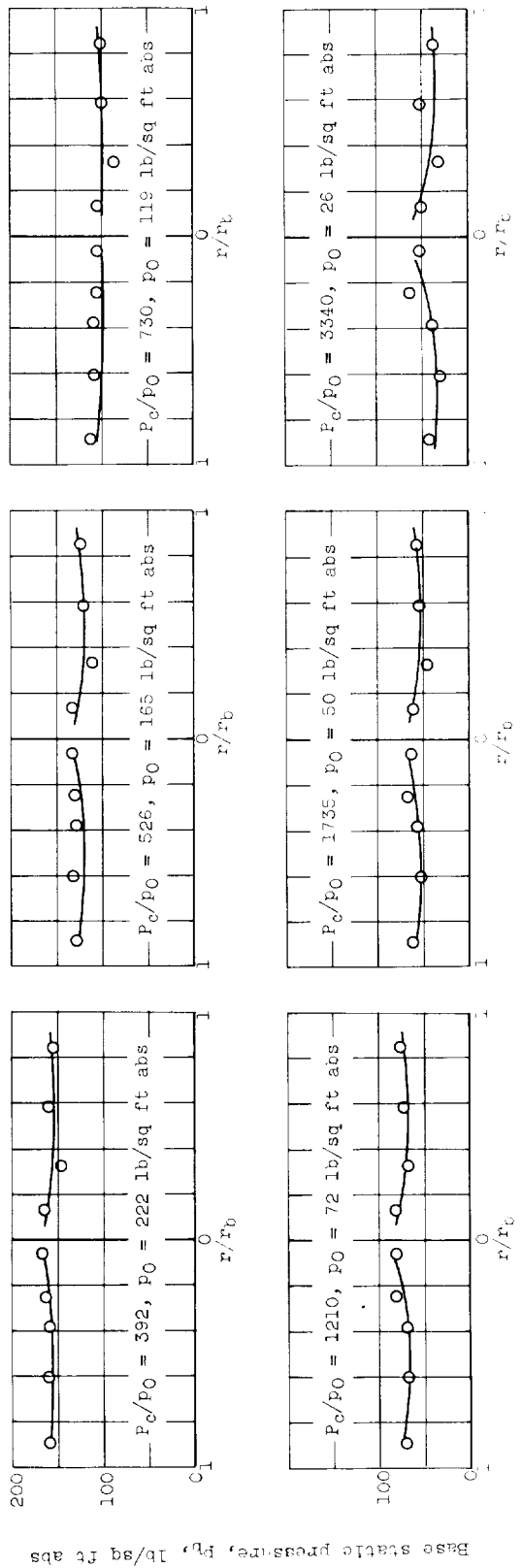


(a) Base heat flux distribution.

Figure 19. - Effect of gimbaling side engines -7° on model base parameters. Nozzle extension ratio  $L/D_e$ , 0.6503; configuration 5.

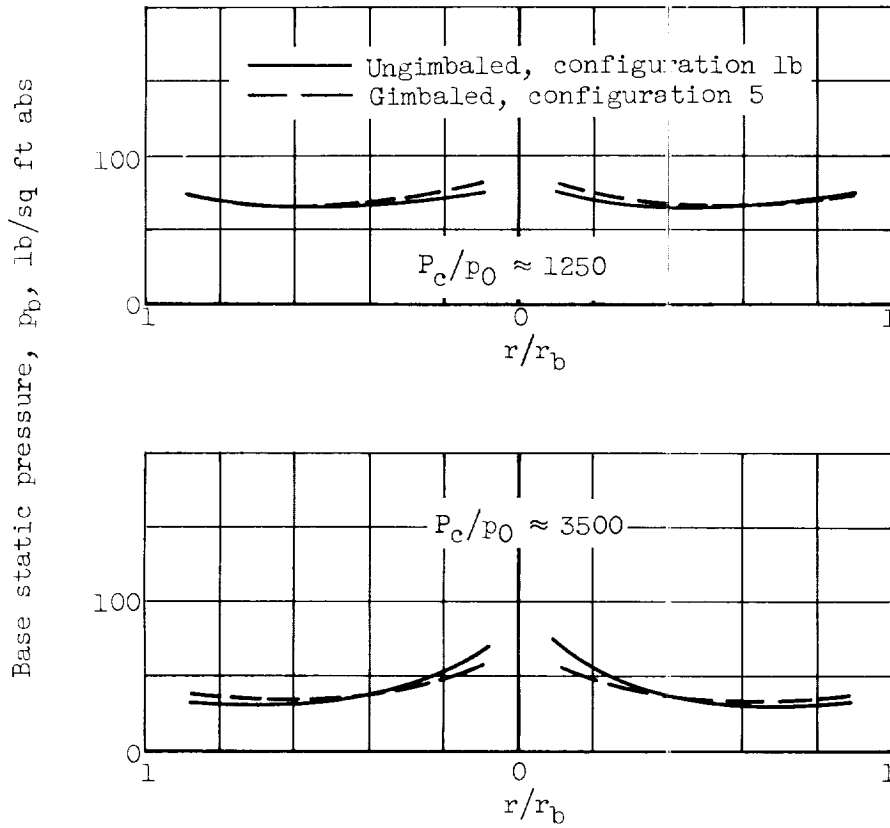


(b) Base temperature parameter distribution. Effect of gimballing side engines - 7° on model base parameters. Nozzle extension ratio  $L/D_e, 0.6503$ , configuration S.



(c) Base pressure distribution.

Figure 12. - Concluded. Effect of gimballing side engines -70 on model base parameters. Nozzle extension ratio  $L/D_e, 0.6503$ ; configuration 5.



(c) Base pressure distribution.

Figure 20. - Concluded. Comparison of gimbaled model base parameters with those of the ungimbaled configuration.



